# Calculation of radiative fluxes from the surface to top of atmosphere based on ISCCP and other global data sets: Refinements of the radiative transfer model and the input data

Yuanchong Zhang,[1] William B. Rossow,[2] Andrew A. Lacis,[2]
Valdar Oinas,[3] and Michael I. Mishchenko[2]

Received 16 December 2003; accepted 24 June 2004; published 6 October 2004.

[1] We continue reconstructing Earth's radiation budget from global observations in as much detail as possible to allow diagnosis of the effects of cloud (and surface and other atmospheric constituents) variations on it. This new study was undertaken to reduce the most noticeable systematic errors in our previous results (flux data set calculated mainly using International Satellite Cloud Climatology Project–C1 input data (ISCCP-FC)) by exploiting the availability of a more advanced NASA Goddard Institute for Space Studies (GISS) radiative transfer model and improved ISCCP cloud climatology and ancillary data sets. The most important changes are the introduction of a better treatment of ice clouds, revision of the aerosol climatology, accounting for diurnal variations of surface skin/air temperatures and the cloud-radiative effects on them, revision of the water vapor profiles used, and refinement of the land surface albedos and emissivities. We also extend our previous flux results, limited to the top of atmosphere (TOA) and surface (SRF), to also include three levels within the atmosphere, forming one integrated vertical atmospheric flux profile from SRF to TOA, inclusive, by combining a new climatology of cloud vertical structure with the ISCCP cloud product. Using the new radiative transfer model and new input data sets, we have produced an 18-year at 3-hour time steps, global at 280-km intervals, radiative flux profile data set (called ISCCP-FD) that provides full- and clear-sky, shortwave and longwave, upwelling and downwelling fluxes at five levels (SRF, 680 mbar, 440 mbar, 100 mbar, and TOA). Evaluation is still only possible for TOA and SRF fluxes: Comparisons of monthly, regional mean values from FD with Earth Radiation Budget Experiment, Clouds and the Earth's Radiant Energy System and Baseline Surface Radiation Network values suggest that we have been able to reduce the overall uncertainties from 10–15 to 5–10 W/m$^2$ at TOA and from 20–25 to 10–15 W/m$^2$ at SRF. Annual mean pressure-latitude cross sections of the cloud effects on atmospheric net radiative fluxes show that clouds shift the longwave cooling downward in the Intertropical Convergence Zone, acting to stabilize the tropical atmosphere while increasing the horizontal heating gradient forcing the Hadley circulation, and shift the longwave cooling upward in the midlatitude storm zones, acting to destabilize the baroclinic zones while decreasing the horizontal heating gradient there. *INDEX TERMS:* 1620 Global Change: Climate dynamics (3309); 3309 Meteorology and Atmospheric Dynamics: Climatology (1620); 3359 Meteorology and Atmospheric Dynamics: Radiative processes; *KEYWORDS:* Earth radiation budget, surface radiation budget (SRB), cloud vertical structure, ERBE, CERES, BSRN

**Citation:** Zhang, Y., W. B. Rossow, A. A. Lacis, V. Oinas, and M. I. Mishchenko (2004), Calculation of radiative fluxes from the surface to top of atmosphere based on ISCCP and other global data sets: Refinements of the radiative transfer model and the input data, *J. Geophys. Res.*, *109*, D19105, doi:10.1029/2003JD004457.

## 1. Introduction

[2] The climate system converts solar radiation into heat and "heat" radiation, water vapor and the circulations of the atmosphere and ocean. The atmospheric circulation causes relatively rapid heat transports (with respect to the oceanic circulation) that integrate local forcing differences and

[1]Department of Applied Physics and Applied Mathematics, Columbia University, New York, USA.
[2]NASA Goddard Institute for Space Studies, New York, USA.
[3]Stinger Ghaffarian Technology, Inc., New York, USA.


0148-0227/04/2003JD004457$09.00

couple the local responses of the other, slower climate components into a single global response, so it is essential to diagnose climate variations globally. However, the climate system is not in static equilibrium. The solar forcing varies strongly on both daily and seasonal timescales; the former timescale is shorter than the response time of the atmospheric circulation (except for the boundary layer and convection) and the latter is longer than the response time of the atmospheric circulation but slower than the response time of the oceanic circulation. Consequently, the atmospheric and oceanic circulations are constantly adjusting (on different timescales) to the changing solar forcing. The ''heat'' radiation is part of the adjustment process. The situation is made more complicated because the atmospheric circulation also redistributes the water vapor and converts some of it into clouds and precipitation, all of which alter the forcing of both the atmospheric and oceanic circulations. These atmosphere redistributions and conversions comprise the ''fast'' feedback processes that mediate the climate's response to changed forcing but they have their foundation in weather-scale (i.e., minutes to days) variations.

[3] To understand how the radiative fluxes are affected by diurnal-to-weather-scale variations in the atmospheric water vapor and clouds, how these variations interact with the atmospheric and oceanic circulations, and how all of these integrate into a climate response, we need to diagnose from observations the radiative flux variations on scales from diurnal and mesoscale to interannual and planetary scale. We have been working for some time [*Rossow and Lacis*, 1990; *Rossow and Zhang*, 1995] to develop global radiative flux data sets with the requisite detail for this purpose. The particular approach we follow is to collect global, weather-resolving measurements that specify all the needed properties of the clouds, atmosphere and surface and to put them into a radiative transfer model to calculate the radiative fluxes at the top of atmosphere (TOA), at the surface (SRF) and at several levels within the atmosphere (ATM), which comprise an integrated vertical atmospheric flux profile (PRF) from SRF to TOA inclusive. After the necessary evaluation of the accuracy of these calculated fluxes against independent measurements, primarily by satellites at TOA and by special radiometers at the surface (since no global ATM flux measurements are available, we are unable to directly verify whole flux profiles yet), these results may be taken as a reconstruction of the long-term (>20 years), global radiation budget resolving weather-scale variations. The major advantage of this more elaborate analysis approach over more direct measurements of radiative fluxes alone (usually with incomplete spatial/temporal coverage) is that we can then directly diagnose the causes of the flux variations because the PRF are integrated with all the separated input physical parameters that generate the fluxes. Moreover, once evaluated, such results also provide a direct check of the radiation model used in (at least) one climate general circulation model (GCM) and an indirect check of the (mostly) satellite-based measurements of the cloud, atmosphere and surface properties that are used.

[4] Since we last reported on our methodology [*Zhang et al.*, 1995] for calculating global, 3-hourly broadband shortwave (SW) and longwave (LW) radiative fluxes at TOA and SRF, the radiative transfer model, the satellite-retrieval algorithms, the available global data products and the independent observations of TOA and SRF radiative fluxes have all improved. The NASA Goddard Institute for Space Studies (GISS) radiative transfer model has undergone many important changes to enhance its capability, increase its accuracy and improve input climatological data sets on the basis of new understanding of the climate system. Likewise, the International Satellite Cloud Climatology Project (ISCCP) has improved its satellite radiance calibrations, cloud retrieval and analysis methods, thereby, reducing various errors/uncertainties and biases in the cloud measurements. The old ISCCP-C-series data sets (CX, C1 and C2 [see *Rossow and Schiffer*, 1991]) have now been replaced by the new D-series data sets (DX, D1 and D2 [see *Rossow and Schiffer*, 1999]), which incorporate more complete cloud properties, particularly concerning ice clouds, and cover a longer time period from July 1983 to the present (now planned to extend through 2006). The independent determinations of TOA and SRF radiative fluxes are much improved with the advent of the Clouds and the Earth's Radiant Energy System (CERES) experiment [*Wielicki et al.*, 1996] and the release of more data from the Baseline Surface Radiation Network (BSRN) [*Ohmura et al.*, 1998].

[5] Consequently, the time has come to advance our flux calculations by using the new 2001 GISS radiative transfer model (the radiation component of the GISS GCM [*Hansen et al.*, 2002]), the new ISCCP data sets, as well as better ancillary data sets that have become available.

[6] In the previous work, our radiative transfer model (*Zhang et al.* [1995], and hereinafter ''95-Model'') was modified from the original radiative transfer model used in the old 1983 GISS GCM Model II as described by *Hansen et al.* [1983], and therefore was its off-line application version. While maintaining all of the original characteristics, 95-Model had some additional optional specifications, could handle a wider variety of physical variables as inputs and provided more detailed output for a wider variety of situations. The primary goal of 95-Model was to use the global satellite-derived cloud properties from the ISCCP-C1 data set [*Rossow and Schiffer*, 1991] with other ancillary data for specifying all the physical properties of the atmosphere and surface to calculate global SW and LW fluxes at TOA and SRF at intervals of 280 km and 3 hours for every third month from April 1985 to January 1989 (the Earth Radiation Budget Experiment (ERBE) period [*Ramanathan et al.*, 1989]). The main resulting data product of 95-Model was called ISCCP-FC. For 95-Model, we conducted an extensive and thorough set of sensitivity and evaluation studies reported by *Zhang et al.* [1995] and *Rossow and Zhang* [1995]. From the comparison of our results with the observations, we concluded that our 95-Model-based fluxes, ISCCP-FC, had overall uncertainties of 10–15 $Wm^{-2}$ and 20–25 $Wm^{-2}$ for regional and monthly mean TOA and SRF fluxes, respectively. For a summary of the most important sensitivity tests of 95-Model, see 2003JD004457-MODEL.txt in the auxiliary material (AM)[1]. Table 1 lists the symbol definitions used in our previous work and throughout this paper.

[1] Auxiliary material is available at ftp://ftp.agu.org/apend/jd/2003JD004457.

**Table 1.** Definition of Symbols Representing the Shortwave, Longwave, and Net Radiative Fluxes for Full-Sky and Clear-Sky Conditions and Overcast Sky[a]

| Symbol | Definition |
|---|---|
| $S\downarrow_t$, $S\downarrow_s$ | downward SW fluxes at TOA and surface, where $S\downarrow_t = \mu_0 S_0$ (cosine zenith angle * solar constant) |
| $S\uparrow_t$, $S\uparrow_s$ | upward SW fluxes at TOA and surface |
| $L\downarrow_t$, $L\downarrow_s$ | downward LW fluxes at TOA and surface (the former is usually set to zero) |
| $L\uparrow_t$, $L\uparrow_s$ | upward LW fluxes at TOA and surface |
| $ALB_t$, $ALB_s$ | planetary albedo (at TOA) and surface albedo |
| $NS_t$ | net SW flux into TOA, equal to $S\downarrow_t - S\uparrow_t$ |
| $NS_s$ | net SW flux into the surface, equal to $S\downarrow_s - S\uparrow_s$ |
| $NS_a$ | net SW flux into the atmosphere, equal to $NS_t - NS_s$ |
| $NL_t$ | net LW flux into TOA, equal to $L\downarrow_t - L\uparrow_t = -L\uparrow_t$ (since $L\downarrow_t = 0$) |
| $NL_s$ | net LW flux into the surface, equal to $L\downarrow_s - L\uparrow_s$ |
| $NL_a$ | net LW flux into the atmosphere, equal to $NL_t - NL_s$ |
| $N_t$ | total net flux into TOA, equal to $NS_t + NL_t$ |
| $N_s$ | total net flux into the surface, equal to $NS_s + NL_s$ |
| $N_a$ | total net flux into the atmosphere, equal to $N_t - N_s$ |
| CLR-$F$ | flux with no cloud cover (and with clear-sky precipitable water for 03-Model), where $F$ is any above symbol, e.g., CLR-$S\uparrow_t$ is the upward SW flux at TOA with 0% clouds |
| CLD-$F$ | flux with 100% cloud cover (and saturated cloud-layer precipitable water for 03-Model), e.g., CLR-$S\uparrow_t$ is the upward SW flux at TOA with 100% clouds (exception: if its full-sky counterpart has no contribution from clouds, i.e., if a grid box has no cloud information, CLD-$F$ = CLR-$F$) |
| CFC-$F$ | cloud flux change (“cloud forcing” as popularly used, see explanation given by *Rossow and Zhang* [1995]), defined as the difference between full-sky and clear-sky, e.g., CFC-$S\uparrow_t = S\uparrow_t -$ CLR-$S\uparrow_t$ |

[a]SW, shortwave; LW, longwave.

[7] Our previous results also identified the key sources of error, the improvement of which was one of the main objectives of this study. First and foremost, characteristic regional discrepancies pointed to biases in the ISCCP-FC fluxes where ice clouds predominated. This bias is associated with the ISCCP-C series treatment of all clouds as composed of liquid spheres. In such locations, $S\uparrow_t$ and $L\uparrow_t$ were too large. With the new ISCCP-D series data, where ice clouds are treated with a separate microphysical model, these biases are expected to decrease. The FC values of $L\uparrow_t$ in the subtropics were systematically too small; since clouds in this region are generally either low level or absent, the problem was thought to be associated with either the total abundance or vertical distribution of the water vapor obtained from the operational Television Infrared Observation Satellite (TIROS) Operational Vertical Sounder (TOVS) data set (produced operationally by NOAA [*Kidwell*, 1995]) or a problem with the radiative model's treatment of water vapor absorption. The main concern for surface fluxes involved the details of calculations of $L\downarrow_s$ and $L\uparrow_s$, particularly their diurnal variations and the cloud effects on the diurnal variations. The previous calculations lacked an estimate of the diurnal variation of near-surface air temperatures ($T_a$) over land and employed the ISCCP determinations of the diurnal variations of the surface skin temperature ($T_s$), which are biased to clear-sky conditions. Last, the FC values of $S\uparrow_t$ and $S\downarrow_s$ were both too high. Aside from problems caused by the ice clouds, this bias appeared in both clear and cloudy sky fluxes, suggesting problems in the aerosol amounts and their optical properties, particularly absorption, and the surface albedos.

[8] The second main objective of this study was to extend the flux calculations at TOA and SRF to whole atmospheric flux profiles (PRF), TOA and SRF inclusive, by exploiting a new climatology of cloud vertical structure (CVS) produced by *Wang et al.* [2000]. Although the climatology has coarse vertical resolution and does not provide instantaneous cloud layer information, we have developed a statistical model by combining this climatology with the ISCCP cloud information to provide an approximate connection between meteorological conditions and the vertical distribution of cloud layers (W. B. Rossow et al., Statistical model of cloud layer vertical structure associated with different cloud types, submitted to *Journal of Climate,* 2004) (hereinafter referred to as Rossow et al., submitted manuscript, 2004).

[9] This paper describes the changes made to 95-Model to produce our new radiative model, hereinafter “03-Model,” along with the input data changes in implementing all of the new improvements of the GISS radiation model. We also summarize our progressing in producing, for the first time, global, long-term, SW and LW radiative flux profiles, combining the SRF, ATM and TOA fluxes [*Zhang and Rossow*, 2002], called the ISCCP-FD product. We compare our new results to the observations from ERBE, CERES, the Earth Radiation Budget Satellite (ERBS) nonscanner data set [*Wielicki et al.*, 2002] and BSRN.

[10] Similar to 95-Model, 03-Model is an application version of the new 2001 GISS GCM radiation model [*Hansen et al.*, 2002; cf. *Oinas et al.*, 2001]. Table 2 compares the main features of 03-Model and 95-Model (for more details, see AM, 2003JD004457-MODEL.txt).

[11] For brevity, we avoid repeating the details of our previous 1995 work unless it is necessary and we concentrate on the most important changes of 03-Model from 95-Model and their corresponding sensitivity tests (section 2), and the changes in the new input data sets (section 3) with respect to those used with 95-Model. With the new 03-Model and new input data sets, the overall flux changes and our new products are described in section 4. Section 5 is our evaluation of our new results by comparisons with both the old observational results used before

**Table 2.** Comparison of the Main Features of the Radiative Transfer Models Used: The New 03-Model and the Old 95-Model[a]

| | Main Features | 03-Model (New) | 95-Model (Old) |
|---|---|---|---|
| 1 | original radiative transfer model | new 2001 NASA GISS GCM radiation model [*Hansen et al.*, 2002; *Oinas et al.*, 2001] | old 1983 NASA GISS GCM radiation model [*Hansen et al.*, 1983] |
| 2 | SW (0.2–5.0 μm) spectral resolution in $k$ | 15 $k$ for CKD | 12 $k$ for CKD |
| 3 | LW (5.0–200.0 μm) spectral resolution in $k$ | 33 $k$ for CKD | 25 $k$ for CKD |
| 4 | UVA and UVB treatment | included | not included |
| 5 | accuracy with respect to line-by-line calculation | 1 W/m$^2$ plus significant improvement for upper stratospheric cooling rates due to $H_2O$ | 1% for cooling rates throughout troposphere and most of stratosphere |
| 6 | VIS surface albedo (0.2–0.7 μm) for Land | aerosol-corrected ISCCP-D1 VIS reflectances in place of GCM's 1-band VIS albedo | ISCCP-C1 VIS reflectance in place of GCM's 1-band VIS albedo |
| 7 | NIR surface albedo (0.7–5.0 μm) for land | ISCCP-D1 VIS reflectance multiplied by revised ratios of 5-band NIR to VIS | ISCCP-C1 VIS reflectance multiplied by revised ratio of 1-band NIR to VIS |
| 8 | broadband SW surface albedo for water | equals new GCM's (with added effects of foam and hydrosols) | revised from old GCM (based on Fresnel reflection with wind speed = 2 m/s) |
| 9 | surface emissivity | nonunit (over 33 spectral $k$) | unit |
| 10 | surface skin temperature | from D1, corrected for nonunit emissivity and diurnally adjusted | from C1 (unit emissivity in retrieval) |
| 11 | surface air temperature | diurnally adjusted and logarithmically extrapolated from TOVS profile | linearly extrapolated from TOVS profile |
| 12 | atmospheric gaseous absorbers | temporally varying vertical profile climatology for 1850–2050 with latitudinal gradients | fixed global mean concentration at 1958/1980 levels |
| 13 | water vapor continuum absorption | temperature dependent from *Ma and Tipping* [1991] and *Tipping and Ma* [1995] | empirical formula from *Roberts et al.* [1976] |
| 14 | aerosols | monthly (tropospheric and stratospheric) vertical profile climatology for 18 species with humidity effects at 5° × 4° for 1950–2000; zonal and monthly mean volcano aerosols from SAGE II | fixed global mean column optical depth for 11 background species for stratosphere and tropospheric land, ocean, and desert |
| 15 | cloud microphysical model | spherical liquid and nonspherical ice using monthly mean particle-size climatology | spherical liquid-only with effective radius 10 μm |
| 16 | cloud LW emissivity | nonunit from GISS model | unit |
| 17 | SW scattering conservation of (clouds + surface) | used | not used |
| 18 | cloud macro-inhomogeneity | implemented (for plane-parallel model) | not available |
| 19 | cloudy scene flux calculation | from 15 types of cloud properties; water vapor is saturated (from clear sky) weighted by cloud fraction | from areal mean cloud properties; water vapor is identical to clear-sky scene |
| 20 | cloud vertical structure | CVS model-B with overlapping; thickness based on 20-year RAOBS | single-layered; thickness based on the work of *Poore et al.* [1995] |
| 21 | main flux products | FD: PRF (including TOA, SRF and 3-level ATM) upward and downward SW and LW, global, 3-hourly of 2.5° equal-area map for 1983–2001 | FC: TOA and SRF upward and downward SW and LW, global, 3-hourly of 2.5° equal-area map for third month, 1985–1989 |

[a]Their fundamentals are from the new/2001 and old/1983 NASA GISS GCM radiation models, respectively; that is, most features are inherited from the original GISS radiation models that use the correlated $k$ distribution method (CKD).

and newer observational results. Section 6 summarizes the status of this radiation budget reconstruction and its uncertainties and provides an overview of the results.

## 2. Changes of the Radiative Transfer Model and Sensitivity Study Results

[12] All the important characteristic changes from 95-Model to 03-Model are listed in Table 2. For the changes of our new model (and inputs, next section), we have also conducted new sensitivity studies in the same fashion as done for 95-Model except that the date chosen for the new studies is 15 July 1986 instead of 15 July 1985. (The date change has no scientific effect on the results since our sensitivity test results are presented as flux changes caused by model or input changes. To link to our previously reported results in the work of *Rossow and Zhang* [1995], we choose 15 July 1986 and 15 January 1987 for daily mean comparison with ERBE.) Table 3 summarizes the new sensitivity test results that we think are relatively more important by showing the global mean and standard deviations of the differences for daily mean SW and LW fluxes at TOA and SRF from individual map grid cells in our standard 280-km equal-area map grid.

[13] Inherited from the new GISS GCM radiative transfer model (hereinafter the GISS model), 03-Model has higher

**Table 3.** Global Mean and Regional Standard Deviations of Changes in Daily Mean Fluxes Caused by Changes of Input Quantities or Radiative Transfer Model Treatment for 15 July 1986[a]

| | Change of Parameter or Method | $\Delta S\uparrow_t$ | $\Delta S\uparrow_s$ | $\Delta S\downarrow_s$ | $\Delta L\uparrow_t$ | $\Delta L\uparrow_s$ | $\Delta L\downarrow_s$ |
|---|---|---|---|---|---|---|---|
| 1 | new GCM's 16/33 $k$ | −1.72 (2.43) | −0.18 (0.67) | −0.56 (1.91) | 3.19 (2.02) | 0.11 (0.13) | −4.17 (3.85) |
| 2 | new GCM's 5 NIR and 1 VIS albedo bands | −1.43 (1.66) | −2.16 (2.33) | −0.38 (0.74) | 0.00 (0.00) | 0.00 (0.00) | 0.00 (0.00) |
| 3 | new ocean albedo (ocean only) | 1.10 (1.23) | 1.75 (1.78) | 0.58 (0.61) | 0.00 (0.00) | 0.00 (0.00) | 0.00 (0.00) |
| 4 | *Ma and Tipping* [1991] and *Tipping and Ma* [1995] $H_2O$ continuum | 0.00 (0.00) | 0.00 (0.00) | 0.00 (0.00) | 0.15 (0.26) | −0.11 (0.12) | −1.94 (1.84) |
| 5 | new aerosol climatology | 0.85 (1.95) | −1.14 (1.96) | −4.98 (6.52) | −0.67 (1.00) | −0.01(0.04) | −0.15 (0.57) |
| 6 | spherical ice particles (versus liquid spheres) | −3.11 (5.45) | 0.21 (0.47) | 1.80 (3.03) | −0.65 (0.92) | 0.02 (0.03) | 0.54 (0.69) |
| 7 | nonspherical ice particles ($\tau$-rescale) | 4.65 (7.65) | −0.81 (2.02) | −6.83 (11.1) | −1.86 (2.62) | 0.06 (0.08) | 1.25 (1.66) |
| 8 | new nonunit cloud emissivity | 0.00 (0.00) | 0.00 (0.00) | 0.00 (0.00) | −1.70 (1.10) | −0.01 (0.03) | 0.60 (0.42) |
| 9 | aerosol correction for $R_s$ | −0.88 (1.82) | −1.29 (2.57) | −0.33 (0.70) | 0.00 (0.00) | 0.00 (0.00) | 0.00 (0.00) |
| 10 | diurnal adjustment for $T_a$ and $T_s$ | −0.00 (0.08) | −0.00 (0.02) | −0.01 (0.08) | −0.49 (1.54) | −4.97 (16.0) | −1.85 (8.06) |
| 11 | SAGE/Oort upper tropospheric T/Q filling | −0.16 (0.36) | −0.02 (0.14) | −0.11 (0.30) | −1.85 (3.96) | 0.00 (0.00) | 0.82 (5.21) |
| 12 | D1 cloud versus C1 cloud input | −3.78 (10.5) | 0.23 (2.67) | 4.35 (12.9) | −0.74 (4.56) | −0.03 (1.93) | 0.37 (7.84) |
| 13 | Cf-weighted vapor saturation for clouds | −0.32 (0.34) | −0.05 (0.10) | −0.36 (0.42) | −0.54 (0.51) | 0.07 (0.09) | 1.15 (1.37) |
| 14 | new RAOBS cloud thickness/base | 0.23 (1.24) | 0.10 (0.42) | 0.63 (1.67) | −0.64 (1.33) | −0.12 (0.20) | −1.98 (3.25) |
| 15[b] | 15-type clouds with new RAOBS base | −1.46 (4.10) | 0.04 (0.79) | 1.21 (4.55) | 1.85 (5.97) | −0.05 (0.21) | −1.06 (3.84) |
| 16 | CVS model versus 1-layer clouds | −0.35 (1.50) | 0.08 (0.53) | 0.29 (1.66) | −1.25 (1.94) | 0.10 (0.16) | 1.83 (2.82) |
| 17 | mesoscale inhomogeneity | −.0.33 (0.35) | 0.02 (0.06) | 0.32 (0.32) | 0.27 (0.34) | −0.01 (0.01) | −0.12 (0.09) |
| 18 | overall FD versus FC | −5.93 (10.8) | −5.06 (8.34) | −5.58 (13.7) | −2.42 (8.45) | −3.41 (19.7) | −6.39 (16.2) |

[a]Values are given in $W/m^2$. T/Q, temperature/humidity.

[b]Note that when this sensitivity test is redone after features 16 and 17 are included, the results become 1.42 (3.70), −0.24 (0.90), −1.95 (4.53), −1.04 (5.71), 0.13 (0.23), and 2.35 (4.11), respectively; that is, all the changes have reversed sign while the magnitudes are of about the same order.

spectral resolution, employing 15 noncontiguous correlated $k$ intervals to model overlapping cloud-aerosol and gaseous absorption for the SW (nominally 0.2–5.0 μm) and 33 noncontiguous correlated $k$ intervals for the LW (nominally 5.0–200.0 μm, including one for a "window" wavelength: 11.1–11.3 μm). In addition, the SW now incorporates distinct UVA and UVB treatments based on off-line line-by-line calculations. The 33-$k$ scheme for the LW is designed to match line-by-line fluxes to within 1 $Wm^{-2}$ and provides a significant improvement for upper stratospheric cooling rates due to water vapor over the old 25-$k$ interval scheme (*Oinas et al.* [2001]; see also AM, 2003JD004457-MODEL.txt). With more $k$ spectral intervals to treat the atmosphere and its constituents, including aerosols and clouds as well as surface properties, 03-Model is expected to have higher accuracy than 95-Model. The sensitivity test of the spectral resolution change (holding all other parameters fixed to 95-Model values) shows (Table 3) that it decreases $L\downarrow_s$ by 4.2 $Wm^{-2}$, increases $L\uparrow_t$ by 3.2 $Wm^{-2}$, and decreases $S\uparrow_t$ by 1.7 $Wm^{-2}$ (other fluxes change by $\leq$0.5 $Wm^{-2}$). From our previous evaluations [*Rossow and Zhang*, 1995], these flux changes are all improvements (bias reductions) with respect to more direct observations.

### 2.1. Revised Treatment of Surface Properties

[14] The new GISS model has revised visible albedo (0.2–0.7 μm) values and has a finer, more precise 5-band near-infrared (NIR: 0.7–5.0 μm) albedo representation for each of 11 "vegetation" types (but 8 of which are used, see *Zhang et al.* [1995]). In addition, two of the "vegetation" types, "rocks" and "desert," have been merged into one type, "sands." Table 3 shows that these changes cause a decrease of 2.2 and 1.4 $Wm^{-2}$ for $S\uparrow_s$ and $S\uparrow_t$, respectively, and a decrease of 0.4 $Wm^{-2}$ for $S\downarrow_s$ for land only (with or without snow). The global mean clear-sky surface albedo (for land) decreases by about 1% compared with the old GISS model.

[15] The 03-Model modifies the 6-band (1 for visible and 5 for NIR) albedos from the new GISS model with a procedure similar to that of 95-Model (but with only 2 bands, 1 for visible and 1 for NIR). The result is that we keep the regression results (with ERBE) for each "vegetation" type but now distributed over the new 5-band NIR land albedos, retaining the spectral characteristics from the new GISS model's NIR albedos. In the flux calculations, the visible and NIR albedo values are obtained by the same method used in 95-Model except (1) ISCCP-C1 visible reflectances ($R_s$) are now replaced by D1 values corrected for aerosol scattering and absorption effects that are neglected in the ISCCP $R_s$-retrieval analysis (the correction employs the new aerosol climatology of the new GISS model that is also included in the flux calculations, see next section), and (2) we now have higher spectral resolution for NIR albedos (5 bands).

[16] For ocean albedo, the effect of foam and hydrosols on ocean albedo is now included in the new GISS model [*Gordon and Wang*, 1994]. The new GISS model has also been revised to account more accurately for albedos at very high solar zenith angles. Table 3 shows the test of the ocean albedo changes. The new GISS model's ocean albedo is used by 03-Model without modification.

[17] All of our radiative models construct the total albedo for each map grid cell as an area-weighted average of the albedos for up to four different subcells (when present: vegetated land, ice-covered land and ocean, and open water), where the albedo of the vegetated land is the area-weighted mean of any of the 8 types present. Snow is an added component to adjust the solid-surface albedo. The spectral and solar-zenith-angle dependence of snow uses the scheme of *Wiscombe and Warren* [1980]. The effects of the changing spectrum of surface solar insolation, caused by clouds and water vapor (and other atmospheric gases), are explicitly accounted for by the radiative transfer model. Note that although they are functions of solar zenith angle, the surface albedos in all of our models

are fixed attributes of the surface (varying with seasons), and sometimes are called "black-sky" or "true" albedo by some authors.

[18] With all of the above changes, 03-Model has a smaller global mean total surface albedo by a little more than 1% than 95-Model (not listed in Table 3), while having larger albedos over both polar regions. In general, these changes improve the comparison of the calculated SW fluxes with more direct observations. (For more details, see AM, 2003JD004457-MODEL.txt.)

[19] Compared with unit surface emissivity used in 95-Model and its input $T_s$ from ISCCP-C1 that was retrieved using unit emissivity, 03-Model uses the full spectral dependence of surface emissivity, together with emissivity-corrected values of $T_s$, in calculating LW fluxes (for more details, see AM, 2003JD004457-MODEL.txt).

[20] All of our models allow for a difference between surface skin temperature ($T_s$) and near-surface air temperature ($T_a$). Because surface LW fluxes are very sensitive to $T_a$ (item 3 in section 2 in AM, 2003JD004457-MODEL.txt), 03-Model determines $T_a$ more accurately using a logarithmic extrapolation from the temperature profile (as function of pressure level) instead of linear extrapolation as used in 95-Model to reduce some unrealistically extreme LW flux values.

### 2.2. Revised Treatment of Atmospheric Properties

[21] In 03-Model the weaker bands of $H_2O$, $CO_2$ and $O_3$, as well as all absorptions by $CH_4$, $N_2O$, CFC-11 and CFC-12 (all CFCs in this section refer to chlorofluorocarbons), are now included approximately as overlapping absorbers. Vertical profiles and latitudinal concentration gradients of $CH_4$, $N_2O$, and CFC are based on the work of *Minschwaner et al.* [1998]. Greenhouse forcing, due to several dozen minor species, CFCs, HFCs, PFCs, HCFCs, etc. [*Jain et al.*, 2000; *Naik et al.*, 2000], is included in the form of equivalent amounts of CFC-11 and CFC-12. In addition, the new GISS model now varies the abundances of these gases with time over the period 1850–2050 based on a compilation of recent measurements with inferences from tracer modeling anchored by in situ measurements and ice core data [e.g., *Hansen and Sato*, 2001] to reflect more complete and updated knowledge.

[22] The 03-Model uses the temperature-dependent absorption coefficients for water vapor continuum absorption from *Ma and Tipping* [1991] and *Tipping and Ma* [1995], which are based on theoretical calculations and perform better in comparison with laboratory measurements. The sensitivity test results are shown in Table 3.

[23] The 03-Model also uses a new GISS global, $5° \times 4°$, monthly mean climatology of aerosol vertical profiles for the stratosphere and troposphere (including a separate dust component), composed of 18 different aerosol size and composition combinations to account for sulfates, sea salt, sulfuric acid, dust, black carbon, and organic carbon aerosols [e.g., *Koch et al.*, 1999; *Koch*, 2001; *Tegen and Lacis*, 1996; *Tegen et al.*, 2000] that varies from month to month over the period 1950–2000 [*Hansen et al.*, 2002]. As shown in Table 3, the largest effect of the aerosol changes is a decrease of 5.0 $Wm^{-2}$ for $S\downarrow_s$. The 03-Model has about twice the aerosol as 95-Model in the global mean total-column optical depth (at 0.55 μm) (for more details, see AM, 2003JD004457-MODEL.txt).

### 2.3. Revised Treatment of Cloud Properties

[24] Although the old GISS model had options for different effective sizes for both spherical liquid and spherical ice cloud particles, 95-Model used spectrally dependent optical parameters (extinction coefficient, single-scattering albedo and phase function) based on the same microphysical cloud model that was used in the ISCCP retrievals, which assumed that all clouds are composed of spherical liquid-water droplets with an effective radius of 10 μm and size distribution variance of 0.1. The new GISS model has an additional option for nonspherical ice cloud (and aerosol) particles based on off-line calculations using ray tracing and T-matrix theory [*Mishchenko et al.*, 1996b]. The new ISCCP-D data also differentiates between liquid and ice clouds, employing a nonspherical ice particle shape to retrieve the properties of ice clouds. However, since the ISCCP retrieval uses a fractal particle shape with an aspect ratio of one, whereas the GISS model uses a particle shape with an aspect ratio of 2, which is a better compromise over all clouds [cf. *Han et al.*, 1999], 03-Model retains the GISS model's ice microphysical model and rescales the asymmetry parameter ($g$) from the fractal to elongated crystal shape (for specific information on the particle shape and size and a justification for this choice of the ISCCP ice particle model, see *Mishchenko et al.* [1996a]). Table 3 shows that introducing a cloud microphysical model with spherical ice particles and effective radii of 30 μm for clouds with top temperatures less than 260 K, instead of the previous 10 μm liquid particles for all clouds, decreases $S\uparrow_t$ by 3.1 $Wm^{-2}$ and increases $S\downarrow_s$ by 1.8 $Wm^{-2}$ (other SW and LW fluxes change by <0.8 $Wm^{-2}$). If the ice cloud particles are nonspherical (with the rescaling of asymmetry parameter) instead, $S\uparrow_t$ increases by 4.7 $Wm^{-2}$ and $S\downarrow_s$ decreases by 6.8 $Wm^{-2}$. Additionally, $L\uparrow_t$ decreases by 1.9 $Wm^{-2}$ and $L\downarrow_s$ increases by 1.3 $Wm^{-2}$ (other fluxes change by <0.9 $Wm^{-2}$). Note that the signs of SW flux changes relative to liquid spheres are opposite for the two different microphysical models of ice clouds (but not for the LW flux changes). This may be explained as follows. For SW, increasing the size of the spherical particles reduces the reflectivity and increases the forward scattering (transmission) of the clouds, whereas the nonspherical ice particles do the reverse. For LW, the difference in scattering also accounts for a small flux change because the nonspherical ice clouds scatter the upwelling flux at their bases a little more effectively than spherical particles. Such flux changes indicate that the details of the microphysical model for ice clouds are important and worth further study. Figures 1a–1d show the daily, zonal mean flux changes produced by both the ice cloud models (spherical, nonspherical) against 95-Model spherical liquid cloud model for $S\uparrow_t$, $S\downarrow_s$, $L\uparrow_t$ and $L\downarrow_s$, respectively.

[25] In 03-Model, the final particle sizes of both the liquid and ice clouds are specified using the climatological monthly mean effective radius climatology retrieved from ISCCP-DX data by *Han et al.* [1994, 1999]. To implement the particle size changes (from the fixed D1 values of 10 μm and 30 μm for liquid and ice clouds, respectively, to Han et al.'s variable values), the ISCCP-D1 cloud optical thickness

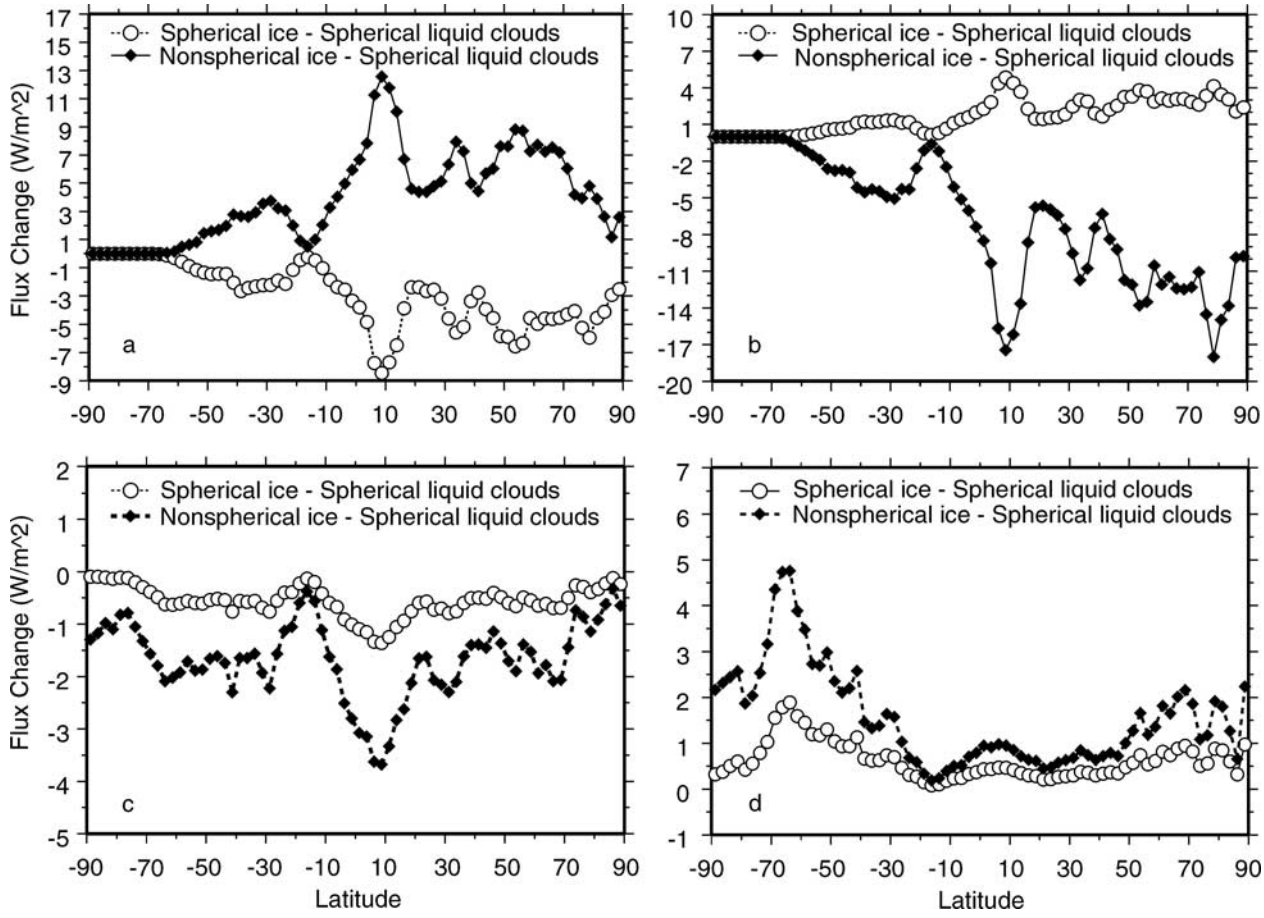


**Figure 1.** Zonal, daily mean flux changes in W/m$^2$ for 15 July 1986 produced by changing cloud microphysical models from spherical liquid to spherical ice cloud particles and from spherical liquid to nonspherical ice cloud particles for (a) $S\uparrow_t$, (b) $S\downarrow_s$, (c) $L\uparrow_t$, and (d) $L\downarrow_s$.

($\tau_c$) values are rescaled to account for the different asymmetry parameters associated with the different sizes (and shapes). Although these details make the calculations more realistic in detail, all of the SW and LW flux changes are <0.2 Wm$^{-2}$ (not listed in Table 3). However, their effect on the $\tau_c$ retrieval is important for improving the ISCCP results.

[26] For consistency with the ISCCP-C retrieval, 95-Model set the LW emissivity of clouds to unity even though the old GISS model had the capability to account for nonunit emissivity. The 03-Model now activates this option to treat clouds more realistically and to remain consistent with the ISCCP-D retrieval that now accounts for nonunit emissivity as well [*Rossow and Schiffer*, 1999]. The thermal fluxes in the GISS radiation models are calculated without multiple scattering, using spectrally dependent Mie theory absorption cross sections, but correction factors for multiple scattering effects to the TOA outgoing flux are included parametrically using tables that have been generated in off-line calculations. The change of the cloud emissivity from unit to nonunit causes a decrease of 1.7 Wm$^{-2}$ and an increase of 0.6 Wm$^{-2}$ for $L\uparrow_t$ and $L\downarrow_s$, respectively (Table 3).

[27] The 03-Model renormalizes the total conservative SW scattering for clouds integrated with the ground to avoid losing energy conservation caused by accumulated calculation errors in layer-by-layer calculations. This change causes an increase of 1.1 and 0.4 Wm$^{-2}$ for $S\downarrow_s$ and $S\uparrow_s$, respectively, and a decrease of 0.9 Wm$^{-2}$ for $S\uparrow_t$ (not listed in Table 3).

[28] The 03-Model still use plane-parallel geometry, but the cloud treatment is now designed to account approximately for the effects of inhomogeneous cloud properties at subgrid scale on the basis of a parameterization derived from a rigorous theoretical analysis evaluated against Monte Carlo simulations of radiative transfer through inhomogeneous cloud density distributions by *Cairns et al.* [1999]. The parameterization retains the plane-parallel homogeneous layer radiative transfer scheme by rescaling its cloud parameters (optical thickness, $\tau_o$, asymmetric factor, $g_o$, and single-scattering albedo, $\omega_o$) according to the relative variance of the cloud particle density distribution. Global maps of monthly mean cloud particle density distribution have been estimated from the ISCCP-D1 cloud climatology [*Rossow et al.*, 2002], which are incorporated into GISS GCM's prognostic cloud optical parameters to simulate subgrid cloud optical depth distributions. In 03-Model, the scaling parameter is derived directly from the ISCCP-D1 optical depth and ice/liquid cloud water path values at each time and place, following the procedure defined by *Rossow*

**Table 4.** Input Data Sources for Calculating ISCCP-FD and ISCCP-FC Radiative Fluxes[a]

| | Input Variable | Source for ISCCP-FD | Source for ISCCP-FC |
|---|---|---|---|
| 1 | solar constant | 1367 W/m$^2$ (with daily variation) | same as FD |
| 2 | cosine solar zenith angle | 3-hour mean derived from 1987 Astronomical Almanac for years 1950–2050 | virtually same as FD |
| 3 | atmospheric gases (excluding ozone) | vertical profile and latitudinal gradients from climatology with 1850–2050 temporal variations | constant abundances fixed at 1958 or 1980 levels |
| 4 | ozone | TOMS (Version 7) with TOVS fill | TOVS |
| 5 | atmospheric aerosols | GISS climatological vertical profiles of 18 species in global $5^\circ \times 4^\circ$ map, monthly means for 1950–2000 for stratosphere and troposphere | GISS climatology of 11 constant species for global-mean stratosphere and continental, oceanic and desert troposphere |
| 6 | Atmospheric temperature profile | TOVS filled with SAGE climatology for pressures <15 mbar | TOVS filled with U.S. standard profiles for pressures <15 mbar |
| 7 | surface air temperature | logarithmic extrapolation from temperature profile with diurnal adjustment | linear extrapolation from temperature profile (no diurnal adjustment) |
| 8 | atmospheric humidity profile | TOVS filled with Oort/SAGE climatology for pressures <310 mbar; low/middle tropospheric profile adjustment | TOVS filled with U.S. standard profiles for pressures <310 mbar |
| 9 | general cloud properties | 15-type clouds from ISCCP-D1 filled from ISCCP-D2 | area-mean cloud properties from ISCCP-C1 filled from ISCCP-C2 |
| 10 | cloud vertical structure (CVS) | cloud type dependent based on zonal, monthly statistical CVS model | 1-layer clouds, no overlap |
| 11 | cloud top temperature/pressure | ISCCP-D1 cloud top temperature filled from ISCCP-D2, linearly interpolated cloud top pressure | ISCCP-C1 cloud top temperature filled from ISCCP-C2, linearly interpolated cloud top pressure |
| 12 | cloud layer thickness/base | 20-year RAOBS climatology as function of month, latitude and cloud top pressure for land and ocean | *Poore et al.* [1995] climatology as function of month, latitude and cloud top pressure for land and ocean |
| 13 | cloud optical depth | ISCCP-D1 filled from ISCCP-D2 | ISCCP-C1 filled from ISCCP-C2 |
| 14 | cloud phase | ice or liquid based on ISCCP-D1 | all liquid |
| 15 | cloud particle size | seasonal climatology by *Han et al.* [1994, 1999] | 10 μm effective radius |
| 16 | cloud particle shape | spherical liquid and nonspherical ice | spherical liquid |
| 17 | surface albedo: VIS (0.2–0.7 μm) | land, from ISCCP-D1 with aerosol adjustment; ocean, from new GISS GCM | land, from ISCCP-C1 (with no adjustment); ocean, old GISS GCM adjusted by ISCCP-C1 |
| 18 | surface albedo: NIR (0.7–5.0 μm) | land, from input VIS multiplyed by 5-band NIR-to-VIS ratio based on ERBE regression; ocean, new GISS GCM | land, from input VIS multiplied by 2-band NIR-to-VIS ratio based on ERBE regression; ocean, old GISS GCM with ISCCP-C1 adjustment |
| 19 | surface skin temperature | ISCCP-D1 filled from ISCCP-D2, corrected for nonunit emissivity with diurnal adjustment for cloud effects | ISCCP-C1 filled from ISCCP-C2 (unit emissivity) |
| 20 | surface emissivity | nonunit from GISS GCM with slight adjustment | unit |
| 21 | land vegetation, snow, sea ice | eight vegetation types and land ice from *Matthews* [1984], snow from NOAA, sea ice from NSIDC [see *Zhang et al.*, 1995] | same as FD |

[a]There are inevitable repetitions of some material in Table 2, but from a different perspective.

*et al.* [2002], for each of 15 types of clouds present. The implementation of this property is described in section 3.

## 3. Changes of Input Data

[29] The main input data set for 03-Model flux calculations (see Table 4) is the ISCCP-D1 data, which includes information about atmospheric and surface properties in addition to the cloud properties [*Rossow et al.*, 1996]. The ISCCP-D series data sets have many improvements over ISCCP-C series (for more detailed discussion, see *Rossow and Schiffer* [1999]), the former reports all of the cloud properties (i.e., cloud amount Cf, top temperature $T_c$, top pressure $P_c$, optical thickness $\tau_c$, phase, water path WP (LWP or IWP for liquid and ice clouds, respectively)), for a total of up to 15 cloud types [see *Rossow and Schiffer*, 1999, Figure 2]. The subgrid-scale inhomogeneity of the clouds is now characterized in the ISCCP-D1 data set by reporting both $\tau_c$, and LWP/IWP, which are just the radiatively weighted and linear averages of the pixel-level optical thicknesses. The other major change in the cloud properties introduced into these new flux calculations is that on the basis of a statistical comparison of the ISCCP cloud top pressures and cloud layer distributions inferred from radiosonde humidity profiles [*Wang et al.*, 2000], each ISCCP cloud type is assigned a specific vertical structure (Rossow et al., submitted manuscript, 2004), which enables us to estimate radiative fluxes at three additional levels in the atmosphere that, together with TOA and SRF fluxes, produce whole integrated vertical flux profiles (PRF). Table 4 compares the input data sets used by ISCCP-FD and ISCCP-FC production, respectively.

### 3.1. Input Surface Properties

[30] As mentioned in section 2.1, 03-Model uses the new GISS model's aerosol climatology both for correcting the

input ISCCP $R_s$ values and calculating the fluxes. The correction uses a look-up table calculated off-line that relates the aerosol-corrected $R_s$ to the original $R_s$ as a function of total aerosol optical thickness. This correction decreases $S\uparrow_s$, $S\uparrow_t$ and $S\downarrow_s$ by 1.3, 0.9 and 0.3 $Wm^{-2}$, respectively, as shown in Table 3.

[31] In the ISCCP-FC calculations, the input surface skin temperature, $T_s$, was taken from the clear-sky composite values of the ISCCP-C1 data set. As discussed by *Rossow and Garder* [1993], these values accurately represent the surface temperature under clear-sky conditions (aside from the emissivity-dependent bias discussed in AM, 2003JD004457-MODEL.txt) but are biased in different ways regionally and seasonally when used to represent $T_s$ for cloudy conditions [cf. *Prigent et al.*, 2003]. The values of $T_s$ from the ISCCP-D1 data set (after correction for nonunit emissivity) have the same deficiency. Likewise, the near-surface air temperatures, $T_a$, which come from daily TOVS data, lack any diurnal variation. Because the details of the interactions of the different diurnal variations of the surface skin and air temperatures and the clouds are key to estimating the exchanges of energy between the surface and atmosphere, the ISCCP-FD calculations incorporate a diurnal adjustment scheme for $T_s$ (and $T_a$, next section) over land areas. Although the smaller (amplitudes generally 1–2 K) diurnal variations of $T_s$ over low-latitude oceans can also be important [cf. *Webster et al.*, 1996], the corresponding variations of $T_a$ are smaller still (see section 5.2 and discussion in the work of *Rossow and Zhang* [1995]), so over oceans we have retained the daily TOVS values of $T_a$, together with the original $T_s$ diurnal cycle amplitude from ISCCP, which will be a small overestimate. Obtaining a more accurate, diurnally resolved skin SST data set is a current focus of research [*Curry et al.*, 2004].

[32] The diurnal adjustment scheme is applied to the land portion of each 280-km grid box at eight local hours (LT = 0000, 0300, ... 2100) based on 5-year-averaged (1985–1989) monthly mean $T_a$ diurnal cycles from the NCEP reanalysis [*Kalnay et al.*, 1996] and 5-year-averaged (1988–1992) $T_a$ diurnal cycles and their relationship with cloud amount observed directly at surface weather stations [*U.S. Department of Commerce*, 1987]. (For details of the formulation, see AM, 2003JD004457-IO.txt.)

[33] Table 3 shows that the diurnal adjustments of $T_s$ (and $T_a$, next section) decrease $L\uparrow_s$ (and $L\downarrow_s$ and $L\uparrow_t$) by 5.0 (2.4 and 0.6) $Wm^{-2}$, respectively. Figure 2a shows the zonal-mean changes of $T_s$ (and $T_a$) due to the adjustment, and Figure 2b shows the corresponding changes of $L\uparrow_s$ (and $L\downarrow_s$). The largest change appears in the zone from 25°N to 80°N, where the land fraction is largest (the test day is in boreal summertime): >2.5 K for $T_s$ (and 4 K for $T_a$), which translates into flux changes >10 $Wm^{-2}$ for $L\uparrow_s$ (and >20 $Wm^{-2}$ for $L\downarrow_s$). Figures 2c and 2d show the global mean (for all map grid cells with land fraction >33%) diurnal variations of the original unadjusted and adjusted values of $T_s$ and $L\uparrow_s$, respectively.

### 3.2. Input Atmospheric Properties

[34] Because the TOVS temperature profiles are sampled only once per day for clear or nearly clear conditions, there is no diurnal variation of $T_a$ present. Using the same climatological parameters employed in the $T_s$ adjustment, we have applied a diurnal adjustment to $T_a$ (and the corresponding temperature of the lowest layer of the TOVS profile; for details, see AM, 2003JD004457-IO.txt).

[35] Table 3 shows that the flux changes associated with the diurnal adjustments of $T_a$ (and $T_s$) and Figures 2a and 2b show the zonal mean changes for $T_a$ (and $T_s$) and $L\downarrow_s$ (and $L\uparrow_s$), respectively. Figures 2e and 2f show the global mean (including only areas with land fractions >33%) diurnal variations of the original unadjusted and adjusted values of $T_a$ and $L\downarrow_s$, respectively.

[36] Figure 2e also illustrates an additional minor diurnal variation of $T_a$ that occurs even without the implementation of the diurnal adjustment procedure. When cloud layers are inserted into the original TOVS profile, the vertical atmospheric layers are accordingly changed such that each cloud layer becomes a physical layer whose top pressure is obtained by linear interpolation from the original temperature profile using the value of $T_c$ [see also *Zhang et al.*, 1995]. When $T_c$ is too small (i.e., < tropopause temperature) or too large (i.e., > all the temperatures in the TOVS profile) with or without an inversion, the original temperature profile is changed in physically reasonable ways to be consistent with the cloud layer information. Meanwhile, the linear interpolation itself introduces some inaccuracy. All of these alternations of the temperature profile cause a small diurnal variation induced by the relayering of about 1 K for $T_a$. To show the importance of this effect, a third curve is shown in Figure 2e for a test case without inserted cloud layers (and without diurnal adjustment), i.e., the original TOVS temperature profile is retained. As expected (and since TOVS is sampled only once per day), this curve is a straight line: constant temperature at all local times. Since the constant temperature is larger than the average base value of the diurnal cycle (meaning that the TOVS profiles are typically sampled at times of day with higher-than-daily-mean temperatures), the diurnal adjustment for this particular date lowers the unadjusted $T_a$ and $T_s$ (and $L\uparrow_s$, $L\downarrow_s$ and $L\uparrow_t$) for most local times and therefore for their global daily means as reported above.

[37] The diurnal adjustments make the variations of the $T_a$ and $T_s$ more physically realistic (cf. Y.-C. Zhang et al., Comparison of different sources of global information about the radiative properties of the ocean and land surface and the near-surface atmosphere used in surface radiative flux calculations, submitted to *Journal of Geophysical Research*, 2004); note particularly that the maximum value of $T_a$ occurs later in the day than for $T_s$. The magnitude of the adjustments can be up to >5 K or 20 $Wm^{-2}$. Further refinement of both $T_s$ and $T_a$ values, especially under cloudy conditions, is needed to determine more accurately the exchanges of energy and water between the surface and atmosphere and their diurnal variations.

[38] For 03-Model, we have merged the upper tropospheric and stratospheric temperature and humidity profiles obtained from a 5-year average of SAGE II data [*Rind and Liao*, 1997; *Liao and Rind*, 1997] for pressures $\leq$200 mbar and from the 10-year *Oort* [1983] climatology for pressures $\geq$300 mbar into a global, monthly mean data set (on our 280-km equal-area map). This merged climatology is then used to fill in the precipitable water (PW) and the temper-

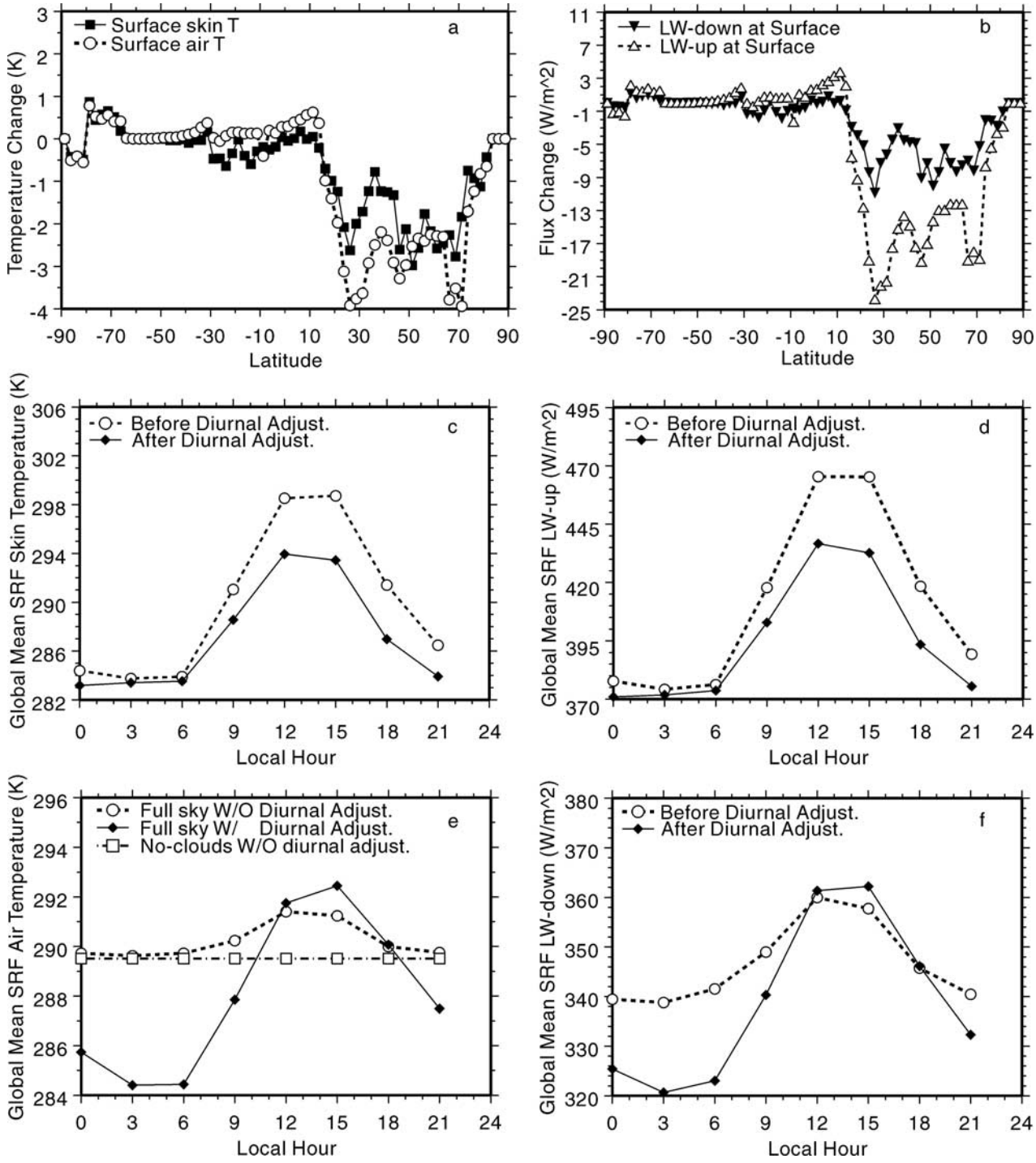


**Figure 2.** (a) Zonal, daily mean changes of $T_a$ and $T_s$ in Kelvin for 15 July 1986 caused by the diurnal adjustment; (b) corresponding changes of $L\downarrow_s$ and $L\uparrow_s$ in W/m$^2$; global mean diurnal variations (for land >33%) for (c) $T_s$ and (d) $L\uparrow_s$ with and without the diurnal adjustment; (e) global mean diurnal variations (for land >33%) for $T_a$ under three different conditions: (1) full sky without diurnal adjustment, (2) full sky with diurnal adjustment, and (3) no clouds and no adjustment; (f) global mean diurnal variations (for land >33%) for $L\downarrow_s$ with and without the diurnal adjustment.

ature profiles wherever TOVS data are missing (see AM, 2003JD004457-IO.txt). Table 3 shows that this profile-filling change causes only slight flux changes.

[39] For cloudy conditions, the PW profile, which is measured for mostly clear-sky conditions, is altered in 03-Model by adding an amount of water vapor in each cloud layer to achieve saturation (100% relative humidity), weighted by cloud fraction (Cf). Water vapor saturation in cloud layers increases the total column water vapor for cloudy scenes by about 5% (e.g., 5% for the monthly mean for July 1986) and causes an increase $L\downarrow_s$ by 1.2 Wm$^{-2}$ (other fluxes change by $\leq$0.5 Wm$^{-2}$) as shown in Table 3.

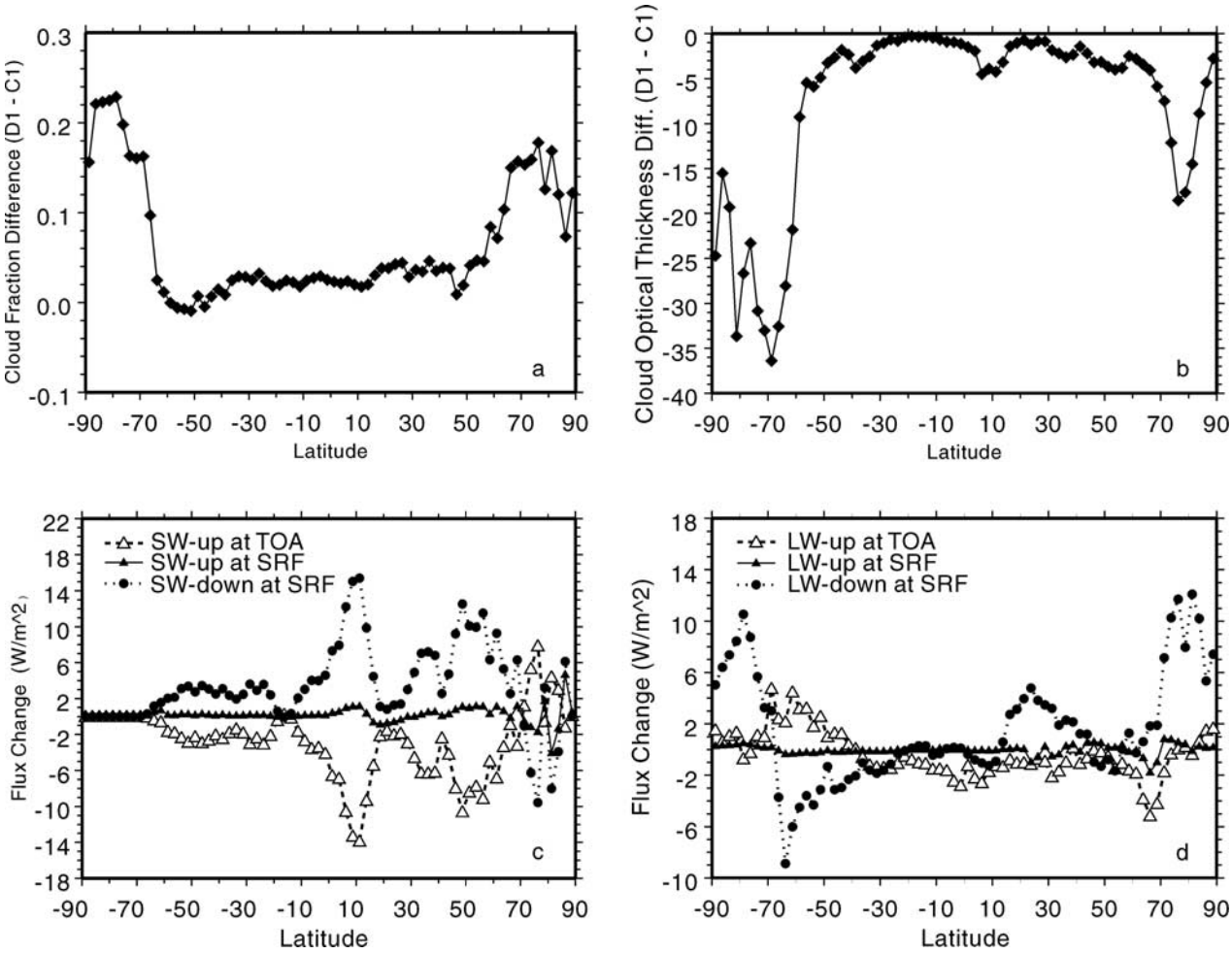


**Figure 3.** Zonal, daily mean differences between D1 and C1 (a) total cloud amounts and (b) cloud optical thicknesses for 15 July 1986; (c) zonal, daily mean changes of $S\uparrow_t$, $S\uparrow_s$, and $S\downarrow_s$ in W/m$^2$ for 15 July 1986 caused by changing cloud properties from ISCCP-C1 to ISCCP-D1; (d) corresponding changes of $L\uparrow_t$, $L\uparrow_s$ and $L\downarrow_s$.

This magnitude increase in the column water vapor for cloudy conditions compared with clear conditions is consistent with the analysis of radiosonde data by *Gaffen and Elliott* [1993].

[40] In the ISCCP-FD flux calculations, the total column ozone abundances are input from the Total Ozone Mapping Spectrometer (TOMS, Version 7) [*McPeters et al.*, 1996] in place of the TOVS values used for the ISCCP-FC calculations; however, when TOMS data are not available (particularly over the wintertime polar regions), the TOVS values are still used. The effect of this change is negligible, <0.1 Wm$^{-2}$ in all fluxes (not listed in Table 3).

### 3.3. Input Cloud Properties

[41] The cloud properties obtained from the ISCCP-D1 data are cloud fraction (Cf), top temperature ($T_c$), top pressure ($P_c$), visible optical thickness ($\tau_c$) and water path (WP). Differences of the map grid mean cloud properties (Cf, $T_c$, $\tau_c$) between ISCCP-C1 and D1 data sets are discussed in the work of *Rossow and Schiffer* [1999]. The most notable changes are as follows: (1) Cf increased by 6% for both polar regions, 7% for northern midlatitudes and 3% for the tropics, mostly over land, (2) $T_c$ decreased by 1.3 K in the global mean (i.e., average cloud tops are higher because the extra detected clouds are thin cirrus), and (3) global mean $\tau_c$ decreased by 1.9 because the optical thickness of ice clouds is lower than for liquid clouds for the same visible reflectance. Figures 3a and 3b show the zonal mean differences between the C1 and D1 values of Cf and $\tau_c$, respectively, for our test date. Replacing the C1 with the D1 cloud properties (still assuming only liquid water clouds) causes a decrease of 3.8 Wm$^{-2}$ for $S\uparrow_t$ and an increase of 4.4 Wm$^{-2}$ for $S\downarrow_s$ while causing negligible changes of the LW fluxes (<1 Wm$^{-2}$) in the global mean. These changes are caused by the lower $\tau_c$ (due to the introduction of the ice clouds) offset by the increase of Cf. Figures 3c and 3d show the zonal mean changes of the SW and LW fluxes caused by the changed input cloud properties (from C1 to D1) with all other inputs identical (same as from D1). In Figure 3c, the changes of $S\uparrow_t$ and $S\downarrow_s$ are nearly mirror images about the zero line. The largest change is near 10°N, where $\tau_c$ decreases the most, by about 4 as shown in Figure 3b. The next largest changes are from about 50°N into the north polar region and near 40°S, both

**Table 5.** Cloud Vertical Structure Model[a]

| Cloud Level | Cloud Type | Subtype | Cloud Vertical Structure | Construction[b] |
|---|---|---|---|---|
| HC | Ci | | 1H | =1-layer cloud |
| HC | Cs | thin | HM* | AM, 2003JD004457-IO.txt |
| HC | Cs | thick | HML | AM, 2003JD004457-IO.txt |
| HC | Cb | | 1-HML | AM, 2003JD004457-IO.txt |
| MC | Ac | thin | 1M | =1-layer cloud |
| MC | Ac | thick | HL* | AM, 2003JD004457-IO.txt |
| MC | As | thin | HL* | AM, 2003JD004457-IO.txt |
| MC | As | thick | ML | AM, 2003JD004457-IO.txt |
| MC | Ns | | ML | AM, 2003JD004457-IO.txt |
| LC | Cu | | 1L | =1-layer cloud |
| LC | Sc | | 1L | =1-layer cloud |
| LC | St | | 1L | =1-layer cloud |

[a]ISCCP-D1's three ranges of optical thickness values (low, middle, and high) and their subtypes (thin/thick) are as follows: For low $\tau_c$, thin is from 0.00 to 1.27, and thick is from 1.27 to 3.55. For middle $\tau_c$, thin is from 3.55 to 9.38, and thick is from 9.38 to 22.63. For high $\tau_c$, thin is from 22.63 to 60.36, and thick is from 60.36 to 378.65.

[b]See AM, 2003JD004457-IO.txt, for some definitions. The cloud top temperature and pressure, $T_c$ and $P_c$, for all new cloud layers (added by the CVS model) are determined either from nearby clouds in the same height category or from the sliding D2 three-year averages. The cloud base pressures, $P_b$, are obtained from the 20-year RAOBS cloud layer thickness climatology. The original total column optical thicknesses, $\tau_c$, are partitioned into all the new cloud layers proportional to each layer's pressure thickness, except for the HM and HL cases (marked by an asterisk in the table), which need adjustment of their optical thicknesses (and cloud inhomogeneity parameter) to maintain consistency with the cloud detection algorithm (see AM, 2003JD004457-IO.txt).

associated with decreases of $\tau_c$ by the introduction of the ice cloud treatment. Near the North Pole, although the cloud fraction has increased by about 10%, the optical thickness decrease dominates the changes. For LW fluxes, the changes are small at most latitudes, but in the polar regions, the increase in cloud amount consists entirely of low-level, even though optically thin, clouds [see *Rossow and Schiffer*, 1999], causing significant changes to $L\downarrow_s$. The sharp decrease of $L\downarrow_s$ at around 65°S is due to a strong decrease of $\tau_c$ in the winter hemisphere. The changes of $L\uparrow_t$ are the opposite sign at high latitudes.

[42] The physical position of each cloud layer is still determined by first interpolating to find the value of $P_c$ based on the value of $T_c$ and then inserting a cloud layer with a finite thickness (giving a cloud base pressure, $P_b$) as done in 95-Model, but using a different and more comprehensive 20-year climatology of cloud layer thicknesses obtained from radiosonde humidity profiles [*Wang et al.*, 2000]. This climatology provides cloud layer thicknesses ($P_b - P_c$) as a function of $P_c$, latitude and month-of-year for land and ocean separately. The change of layer thickness climatologies, when used with map grid cell mean cloud properties, causes a decrease of 2.0 $Wm^{-2}$ for $L\downarrow_s$ (other fluxes change <0.6 $Wm^{-2}$) as listed in Table 3.

[43] In the flux calculations with 95-Model, the input cloud properties (Cf, $T_c$, $\tau_c$) were the radiatively weighted area-average values for each ISCCP-C1 map grid cell (about 280 km in size), which ignored the detailed variations of cloud properties at smaller spatial scales [cf. *Rossow et al.*, 2002] and distorted the relationship between optical thickness and emissivity [cf. *Stubenrauch et al.*, 1999]. This approach was necessitated by the fact that the properties of each of the individual cloud types, defined by the values of $P_c$ and $\tau_c$, were not available in the C1 data set. In the ISCCP-D1 data set, in addition to the area mean cloud properties, the properties for each of the individual cloud types defined by $P_c$-$\tau_c$ categories (see *Rossow and Schiffer* [1999, Figure 2]; see also AM, 2003JD004457-IO.txt) are available. There are nine $P_c$-$\tau_c$ categories, with either liquid or ice clouds possible for low-level and middle-level clouds, giving 15 types of clouds. In 03-Model flux calculations, we calculate fluxes for each cloud type present (and always for clear sky) for every D1 grid cell.

[44] Calculating the area-average fluxes from the Cf-weighted average of the fluxes for the individual cloud types is more accurate than preaveraging the cloud properties themselves because the relationships between cloud properties and fluxes are not linear [cf. *Stubenrauch et al.*, 1999]: This approach better preserves the consistency between the SW and LW fluxes. In the global mean, the change from preaveraged cloud properties to averaging fluxes for the individual cloud types decreases $S\uparrow_t$ by 1.5 $Wm^{-2}$ and increases $S\downarrow_s$ by 1.2 $Wm^{-2}$, while increasing $L\uparrow_t$ by 1.9 $Wm^{-2}$ and decreasing $L\downarrow_s$ by 1.1 $Wm^{-2}$ ($S\uparrow_s$ and $L\uparrow_s \leq 0.05$ $Wm^{-2}$) as shown in Table 3 (for further discussion, see AM, 2003JD004457-IO.txt).

[45] The main input data set, ISCCP-D1, typically has about 15% empty grid boxes (the equal-area map has a total of 6596 cells). A procedure similar to 95-Model is used to fill all the empty cells for the cloud properties (Cf, $T_c$, $\tau_c$, LWP/IWP, and the surface properties $T_s$ and $R_s$), but now the filling is extended to the 15-type cloud properties (with additional LWP/WP) using ISCCP-D2. In addition, the filling now uses a sliding 3-year D2 climatology (instead of fixed 3-year); for example, 2000 D1 is filled by the D2 average over 1999–2001 (but the first and last year are filled by the nearest 3-year-mean D2). As a result of the filling procedure, ISCCP-FD is also globally complete, which produces better global-mean estimates.

[46] Up to this point, all of the sensitivity tests have been performed with the same 1-layer cloud morphology with no overlap as in 95-Model. However, since cloud vertical structure (CVS) is the key to determining the radiative (and latent) heating rate profile in the atmosphere that drives the atmospheric circulation, we exploit the availability of the 20-year climatology of CVS [*Wang et al.*, 2000] to provide the first comprehensive estimates of the atmospheric radiative heating rate profiles. In these calculations, we use a statistical CVS model (Rossow et al., submitted manuscript, 2004) based on reconciling the 1990–1992

climatological layer cloud amounts from the ISCC-D2 and the radiosonde humidity profile observations (RAOBS) [*Wang et al.*, 2000]. The model relates the clouds in each of three levels in the atmosphere to a specified CVS as a function of their $\tau_c$ as follows. All the original ISCCP low cloud types remain 1-layer, low-level clouds (1L). The ISCCP middle cloud types are 1 layer (middle level = 1M), 2 layer (high level and low level = HL) or 2 layer (middle level and low level = ML). The ISCCP high cloud types are 1-layer (high level = 1H), 2-layer (high level and middle level = HM), 3-layer (high/middle/low levels = HML) or 1-thick-layer cloud from the top to a base near the surface. Table 5 describes how this model is constructed.

[47] For the new cloud layers added below/above those directly reported in the ISCCP data set, their physical position is determined either from the $T_c$ values of clouds in the same category reported elsewhere in the original D1 grid cell or from the 3-year average $T_c$ values for the same cloud type and grid box (from the filling procedure), and $P_b$ is determined as explained above. The original values of $\tau_c$ (except in the case of HM and HL, see discussion in AM, 2003JD004457-IO.txt) are partitioned among the new set of cloud layers, proportional to their pressure thicknesses ($P_b - P_c$), preserving the total column values.

[48] Finally, the $\tau_c$ values are adjusted to account for any changes of microphysics from the original ISCCP analysis involving phase changes required by altitude changes as follows. (1) If the original phase is ice (ISCCP labels all clouds with $T_c < 260$ K as ice) and both $T_c$ and $T_b$ are <273.15 K, then the whole cloud layer remains ice. (2) If phase information is not available from the original ISCCP analysis (i.e., it is a newly interpolated or overlapped cloud layer), then if both $T_c$ and $T_b < 273.15$ K, it is also an ice cloud. (3) Otherwise, the cloud is liquid (e.g., some portion of $\tau_c$ of what was originally an ice cloud may be assigned to a lower layer that is liquid). (4) In case of mixed phases where steps 1–3 are not applicable, the cloud layer is split into two single-phase layers (e.g., $T_c < 273.15$ but $T_b > 273.15$, the original cloud layer is divided into two at the 273.15 K level with ice cloud above and liquid cloud below). In all cases where the phase has changed from the original ISCCP label, the value of $\tau_c$ is rescaled to account for the changed microphysics while preserving consistency with the original ISCCP radiance observations. Table 3 shows that introducing the CVS model causes a decrease of 1.3 $Wm^{-2}$ for $L\uparrow_t$ and an increase of 1.8 $Wm^{-2}$ for $L\downarrow_s$ (others fluxes change <0.4 $Wm^{-2}$).

[49] Figure 4a shows the zonal mean changes caused by the new CVS for $S\uparrow_t$ and $S\downarrow_s$, and Figure 4b shows those for $L\uparrow_t$ and $L\downarrow_s$. The SW flux changes are generally very small at lower latitudes (consistent with earlier studies showing the relative unimportance of cloud vertical distribution to SW fluxes in the work of *Zhang et al.* [1995] and *Chen et al.* [2000]; most of the difference is caused by a different partitioning of cloud and water vapor absorption), but they increase to $\geq$2 $Wm^{-2}$ at high latitudes (the South Pole is not illuminated on the test date). For the LW fluxes, prominent changes appear in both tropical and high-latitude regions, up to >2 $Wm^{-2}$ and 3–4 $Wm^{-2}$ for $L\uparrow_t$ and $L\downarrow_s$, respectively, caused mostly by the creation of transparent high-level clouds from some cloud originally labeled as middle level and by the general lowering of cloud base caused by

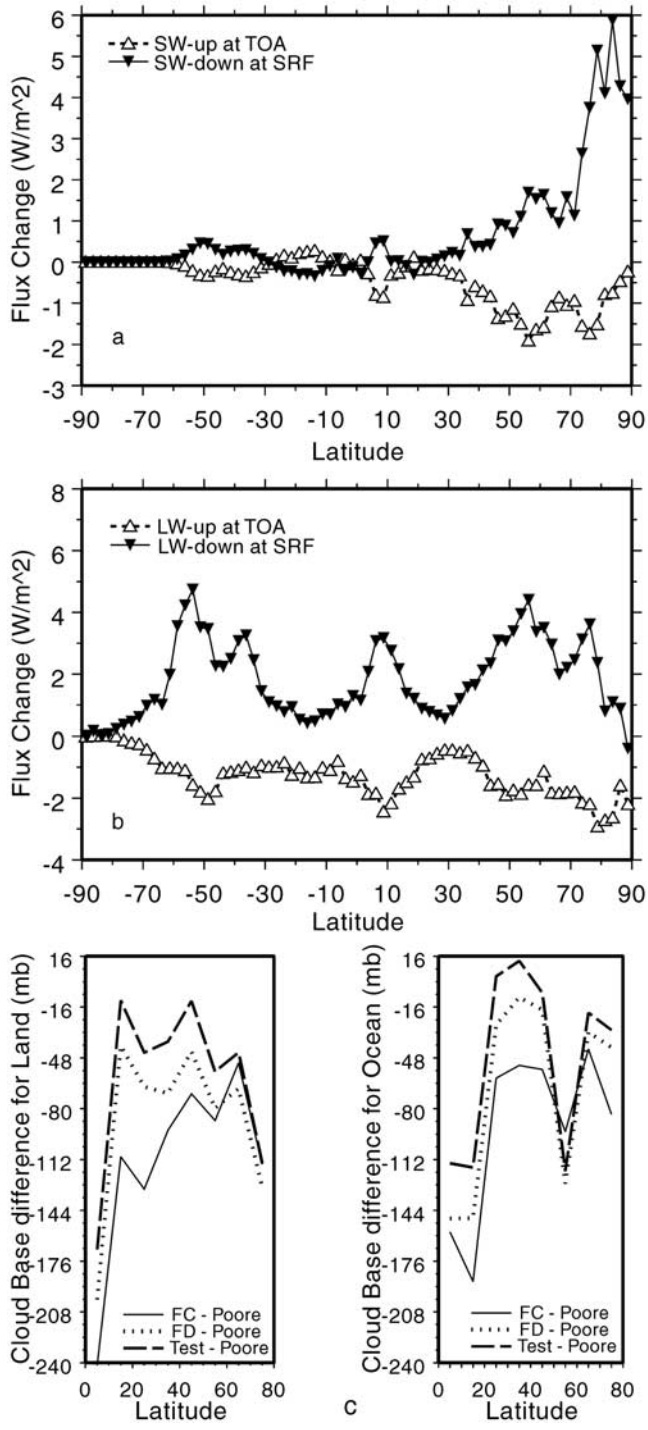


**Figure 4.** (a) Zonal, daily mean changes of $S\uparrow_t$ and $S\downarrow_s$ in $W/m^2$ for 15 July 1986 produced by changing from a 1-layer, nonoverlapped cloud structure to the new cloud vertical structure climatology that includes overlapped cloud layers; (b) corresponding changes of $L\uparrow_t$ and $L\downarrow_s$; (c) associated changes in the bias in zonal, daily mean cloud base pressures from the ISCCP-FC (solid curves) to ISCCP-FD (dotted curves) products. The test case (dashed curves) determines the average cloud base pressure by assuming that 30% of cirrus clouds are not included in the ISCCP-FD average to account for cirrus missed by the radiosondes.

adding cloud layers below those observed from satellites. The solid (dotted) curves in Figure 4c show the difference between the average cloud base pressures in the ISCCP-FC (ISCCP-FD) results when compared with the *Poore et al.* [1995] climatology. However, further analysis of the radiosonde data shows that it tends to overestimate the cloud base pressure for low clouds [*Wang et al.*, 1999] and that it underestimates the amount of thin cirrus by some 20–30% [*Wang et al.*, 2000], both of which lead to an overestimate of average cloud base pressure. As a test of the effect of these RAOBS biases, the dashed curves in Figure 4c shows a new estimate of the average cloud base pressure bias in the ISCCP-FD results when 30% of the cirrus are removed: Generally, average cloud base pressures are biased low by about 50 mbar, except in the deep tropics, where the bias is about 150 mbar, but some of this is caused by the overestimate in the radiosonde results for humid boundary layers. Overall, the remaining bias in $P_b$ is probably <100 mbar.

[50] As mentioned above (and in section 2.3), the effects of realistic three-dimensional inhomogeneities in the cloud mass distribution can be approximated in our plane-parallel model by rescaling the optical parameters of the homogeneous cloud (optical thickness, asymmetric factor and single-scatter albedo). The 03-Model uses the formulae of *Rossow et al.* [2002] to perform the correction for the inhomogeneity of all cloud types. Table 3 shows that the effect of introducing this correction is <0.5 $Wm^{-2}$ for all the SW and LW fluxes. The largest cloud heterogeneity effects appear in the Intertropical Convergence Zone (ITCZ) (not shown), where the most extreme mixtures of convective and cirrus clouds are common. Note that we have actually already included most of the spatial inhomogeneity effect in the flux calculations by treating each cloud type separately; if we had used the area-mean cloud properties, the magnitude of the correction would be larger as shown by *Rossow et al.* [2002]. (For more details, see AM, 2003JD004457-IO.txt.)

## 4. Flux Changes From ISCCP-FC to FD

[51] After incorporating all the changes for the new radiative transfer model and the new input data sets as described, we use 03-Model to calculate radiative fluxes at five levels from SRF to TOA inclusive, globally every three hours over an 18-year period (July 1983 to June 2001). To provide a quantitative summary of the overall flux changes from ISCCP-FC to ISCCP-FD, the last line in Table 3 compares these two results: All three SW flux components ($S\uparrow_t$, $S\uparrow_s$ and $S\downarrow_s$) decrease by about 5–6 $Wm^{-2}$, while the three LW flux components ($L\uparrow_t$, $L\uparrow_s$, and $L\downarrow_s$) decrease by 2.4, 3.4 and 6.4 $Wm^{-2}$, respectively. The CLR-$S\uparrow_t$ decreases by 1.9 $Wm^{-2}$ and CLR-$L\uparrow_t$ increases by 2.1 $Wm^{-2}$ (not listed in Table 3). Figures 5a and 5b show the daily (same day for the sensitivity tests), zonal mean changes of the SW and LW fluxes, respectively, and Figures 5c and 5d show their clear-sky counterparts. The substantial increases of the reflected SW fluxes at both TOA and SRF over the north polar region are primarily due to surface albedo changes associated with changed cloud detections (compare AM, 2003JD004457-FIGURE03.eps, with AM, 2003JD004457-README.txt), while the second largest changes are mostly due to the new aerosol climatology (compare AM, 2003JD004457-FIGURE07.eps, with AM, 2003JD004457-README.txt). For LW, notable changes of $L\downarrow_s$ (Figure 5b) and CLR- $L\downarrow_s$ (Figure 5d) over the southern polar regions are primarily due to an increase of input water vapor amount (partly from change of upper tropospheric PW and partly from the correction of the programming error in previous TOVS data processing (as explained in AM, 2003JD004457-IO.txt)): The clear-sky total column PW increased by 75% from ISCCP-FC to FD (Figure 5e) though the absolute increase is generally <1 mm (except from 58°S to 68°S, where a peak increase of ~2 mm occurs, not shown). An increase of low-level cloud amounts in the winter polar regions also contributes to the increase of $L\downarrow_s$. The large changes of alternating sign over the subtropics and high latitudes in the northern hemisphere are mainly due to the diurnal adjustment of $T_a$ and $T_s$ (compare Figure 2b). All of the other SW and LW flux differences between FC and FD are caused by a complex mix of all the changes of the model and inputs described in the previous sections and cannot be attributed to any single dominant factor. All of these changes are generally improvements of the new flux results compared with the old results as we will see in the following section.

[52] With the introduction of the CVS model, whole integrated atmospheric vertical flux profiles (PRF, TOA and SRF inclusive) are calculated and included in the ISCCP-FD products. Although 03-Model can report fluxes at 20-mbar vertical intervals (linearly interpolated from the physical cloud/air layers), we only save fluxes at five levels (see below) consistent with the relatively coarse vertical resolution of our CVS model.

[53] The ISCCP-FD data set provides global radiative flux profiles (PRF) at temporal intervals of 3 hours (0000, 0300, ... 2100 UTC, the same as the ISCCP-D1 data), horizontal intervals of about 280 km on an equal area map, and five pressure levels (SRF, 680 mbar, 440 mbar, 100 mbar and TOA). Currently this product covers the period from July 1983 to June 2001, but it will be extended as more ISCCP data become available (through at least 2006). At each level, we report the SW and LW, upwelling and downwelling, full-sky and clear-sky fluxes (overcast fluxes can also be derived using the reported cloud amounts) for all cloud types present. In addition, the data set also contains various summaries of the physical quantities that are used in the flux calculation as discussed in the previous sections (see AM, 2003JD004457-IO.txt). All of the detailed information for ISCCP-FD data sets is readily available and information about them can be found at the ISCCP website (http://isccp.giss.nasa.gov/projects/flux.html), where global, monthly/annual-mean climatological maps for relatively important parameters (e.g., all net fluxes and their cloud effects) are also available (and not presented in this paper).

## 5. Evaluation of the New Results

[54] In our previous work [*Rossow and Zhang*, 1995], we summarized our validation studies and its flux products, ISCCP-FC, and CX-derived fluxes, FCX, based on comparisons with ERBE fluxes at TOA and various direct measurements of fluxes (mostly SW) at the surface. To provide the uncertainty estimates for our new products (ISCCP-FD, and DX-derived fluxes, FDX), we have compared them not only

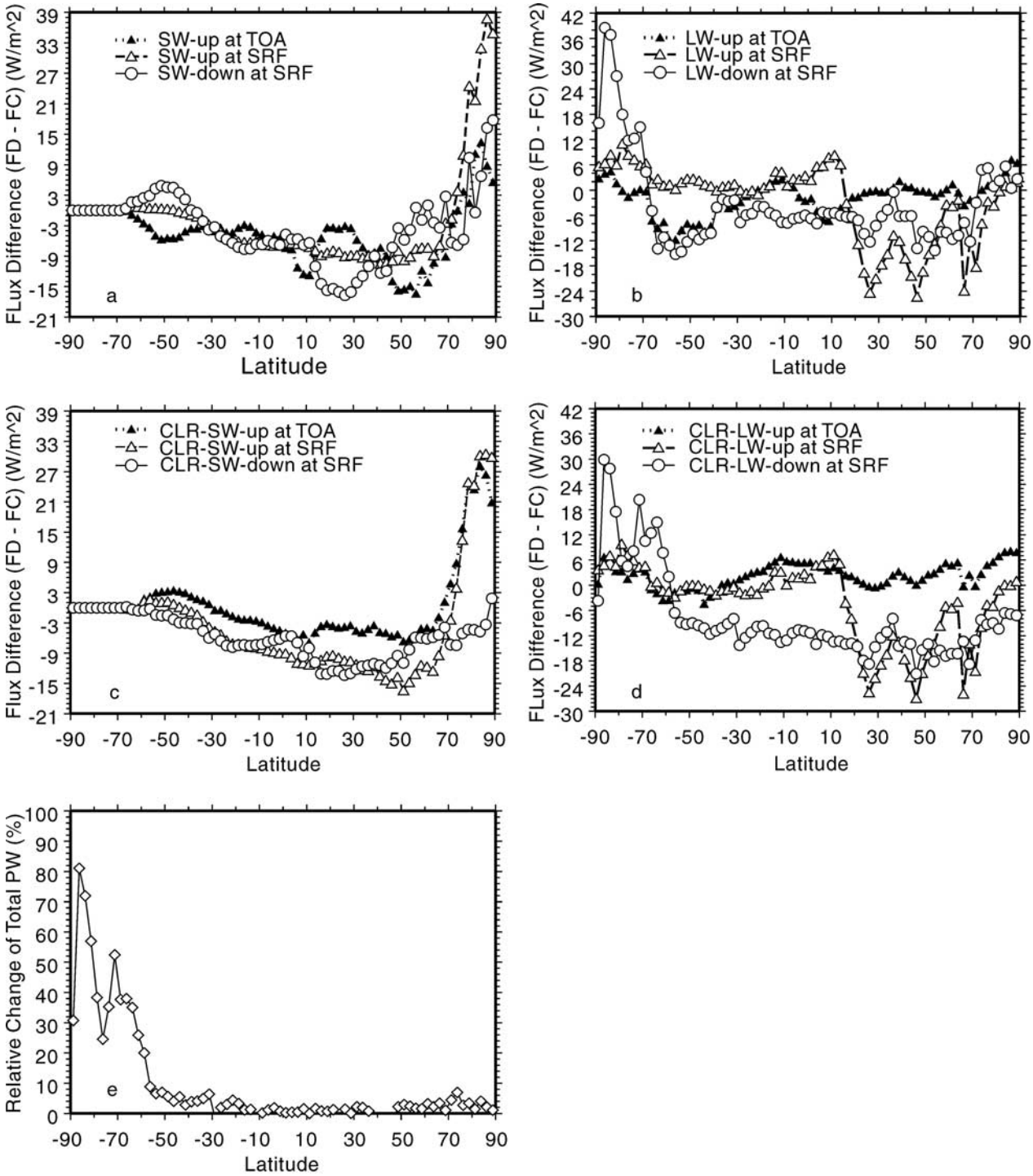


**Figure 5.** (a) Zonal, daily mean changes of $S\uparrow_t$, $S\uparrow_s$ and $S\downarrow_s$ in W/m$^2$ for 15 July 1986 produced by changing from 95-Model to 03-Model, i.e., from ISCCP-FC to ISCCP-FD; (b) corresponding changes of $L\uparrow_t$, $L\uparrow_s$ and $L\downarrow_s$; (c and d) same as Figures 5a and 5b, respectively, but for clear sky; (e) zonal, daily mean relative change of input clear-sky total column PW (%) from ISCCP-FC to ISCCP-FD.

with the same data sets used before (except for four special cases for FCX), but also with the following important newly available observations: (1) the ERBE-like data set from CERES; (2) the 15-year flux anomalies from ERBS non-scanner data set for the tropical zone; (3) BSRN; (4) the surface measurements from 20 cruises in the SeaFlux data collection [*Curry et al.*, 2004].

[55] As emphasized by *Rossow and Zhang* [1995], strict comparisons between the calculated fluxes based on satellite-retrieved physical parameters and the in situ or derived

**Table 6.** Summary of Global Monthly Mean Comparison Statistics at Top of Atmosphere From Grid-Matched Comparisons Between ISCCP-FD and ERBE for 16 Midseasonal Monthly Means (Hour) From April 1985 to January 1989 as Well as the Comparison Between ISCCP-FD and the ERBE-Like CERES Products for 16 Consecutive Months From March 2000 to June 2001[a]

| | Global Average | | | | Regression | | | |
|---|---|---|---|---|---|---|---|---|
| Quantity | ERBE | FD(Type) | Mean Difference (FD − ERBE) | Standard Deviation | Corr. Coef. | Slope | Intercept | Norm. Dev. |
| $S\downarrow_t$ | 351.9 | 352.4 | 0.45 | 1.94 | 1.000 | 0.997 | 0.58 | 1.22 |
| $S\uparrow_t$ | 102.5 | 107.2 | 4.67 | 8.33 | 0.983 | 0.981 | −2.71 | 5.74 |
| $\text{Alb}_t$, % | 29.1 | 30.4 | 1.42 | 2.69 | 0.976 | 0.986 | −0.97 | 1.90 |
| CLR-$S\uparrow_t$ | 53.7 | 54.7 | 0.94 | 11.67 | 0.943 | 1.015 | −1.68 | 8.09 |
| CLR-$\text{Alb}_t$, % | 15.3 | 15.5 | 0.51 | 4.22 | 0.930 | 0.994 | −0.44 | 2.95 |
| $\text{NS}_t$ | 249.4 | 245.2 | −4.27 | 8.14 | 0.997 | 1.003 | 3.55 | 5.73 |
| CLR-$\text{NS}_t$ | 298.2 | 297.7 | −0.51 | 11.90 | 0.994 | 0.982 | 6.09 | 8.34 |
| $L\uparrow_t$ | 235.4 | 233.2 | −2.19 | 5.25 | 0.991 | 1.072 | −14.60 | 3.18 |
| CLR-$L\uparrow_t$ | 267.7 | 262.1 | −5.55 | 7.09 | 0.980 | 1.084 | −16.41 | 4.38 |
| $N_t$ | 14.0 | 12.0 | −1.93 | 8.83 | 0.994 | 0.988 | 2.05 | 6.20 |
| CLR-$N_t$ | 30.5 | 35.6 | 5.64 | 12.27 | 0.991 | 0.969 | −4.27 | 8.41 |
| CFC-$\text{SW}_t$ | −48.8 | −52.5 | −3.85 | 12.39 | 0.931 | 1.008 | 4.17 | 8.65 |
| CFC-$\text{LW}_t$ | 32.3 | 28.9 | −3.06 | 6.59 | 0.933 | 1.061 | 1.49 | 4.46 |
| CFC-$N_t$ | −16.5 | −23.6 | −7.30 | 11.85 | 0.903 | 0.940 | 5.71 | 8.47 |
| | Global Average | | | | Regression | | | |
| Quantity | CERES | FD(Type) | Mean Difference (FD − CERES) | Standard Deviation | Corr. Coef. | Slope | Intercept | Norm. Dev |
| $S\uparrow_t$ | 98.6 | 104.8 | 6.18 | 9.27 | 0.974 | 1.00 | −5.00 | 6.49 |
| CLR-$S\uparrow_t$ | 48.7 | 53.3 | 4.51 | 12.93 | 0.915 | 0.91 | 0.07 | 9.19 |
| $L\uparrow_t$ | 238.8 | 234.4 | −4.40 | 5.55 | 0.989 | 1.07 | −6.89 | 3.43 |
| CLR-$L\uparrow_t$ | 269.0 | 262.4 | −6.62 | 6.58 | 0.977 | 1.03 | 4.92 | 4.47 |

[a]ERBE has two kinds of monthly means, namely, monthly mean (hour) and monthly mean (day). The former first averages over all the days of a month for each of 24 hours and then averages over the 24 monthly hourly means. The latter first averages over 24 hours for each day of a month and then averages all the days of the month. For most months the two results exhibit negligible differences, but there are three months (July 1985, October 1985, and January 1986) of the sixteen for which clear-sky LW monthly (day) has substantially fewer data grid boxes. Therefore, for monthly comparisons, we now use the monthly mean (hour) to have a better comparison for clear sky. Each pair of values contains the coordinates of a point in a scatterplot with ERBE/CERES values on the ordinate and ISCCP-FD values on the abscissa. Regression statistics are from a linear least squares fit to the scatter of points. All values are in $\text{W/m}^{-2}$, except the correlation coefficients and slopes, which are unitless, and the albedos, which are in percent. "Norm. dev." is the RMS distance of all the points from the regression line. Corr. coeff., correlation coefficient. The above definitions for all statistical comparisons are used throughout the text and all tables in this paper.

measurements can rarely be achieved because none of the measurements directly represents what is calculated, and in particular, none of the measurements really match the space-time sampling of the input data sets used. However, we have conducted a number of tests to find the best space-time match for more physically meaningful comparisons and employ the same approach here.

### 5.1. Comparison With TOA Flux Measurements

[56] *Rossow and Zhang* [1995] examined possible sources of uncertainty in the ERBE flux results, which rely on some empirical models (the scene-dependent angle models and a diurnal interpolation model). In addition, the global coverage of the monthly mean ERBE flux product is usually incomplete, particularly for clear-sky components, with the missing regions varying from month to month and from parameter to parameter, and as a result, the ERBE global, annual mean total net flux varies year-to-year by 5–6 $\text{Wm}^{-2}$ (see discussion given by *Rossow and Zhang* [1995]). The published estimate of the RMS uncertainty of the ERBE global, monthly mean fluxes is 3–5 $\text{Wm}^{-2}$ [*Wielicki et al.*, 1996], with regional monthly mean uncertainties being larger. Table 6 shows our new comparison of hourly-monthly means between ISCCP-FD and ERBE based on comparisons for 16 midseasonal months from four years (from April 1985 to January 1989, every third month) for grid-cell-matched global maps (compare ISCCP-FC versus ERBE, by *Rossow and Zhang* [1995, Table 3]). The mean difference of $S\downarrow_t$ for (FD − ERBE) is a little larger than (FC − ERBE): increasing to 0.45 from 0.26 $\text{Wm}^{-2}$; this change occurred because we adjusted our averaging method for the 3-hour-mean cosine solar zenith angle (see AM, 2003JD004457-IO.txt). All the other SW flux biases (FD − ERBE) have decreased by more than half: $S\uparrow_t$ and CLR-$S\uparrow_t$ now have biases of 4.7 and 0.9 $\text{Wm}^{-2}$, respectively, compared with 10.7 and 4.1 $\text{Wm}^{-2}$ for FC. The RMS differences are about the same but the correlation coefficients and the slope/intercepts from the scatterplots are improved, indicating improvement in regional agreement. The largest regional biases of $S\uparrow_t$ are about 15 $\text{Wm}^{-2}$ too high (relative to ERBE) over marine stratus and some coastal regions and about 15 $\text{Wm}^{-2}$ too low over some tropical rainforests and the high Greenland and Antarctic ice sheets. Compared with FC versus ERBE, the global mean albedo bias has also decreased by more than a half: from 3.3% to 1.4% for full sky and from 1.2% to 0.5% for clear sky. For LW fluxes, the major improvement is in the clear-sky component: The bias is now reduced to −5.6 $\text{Wm}^{-2}$ from −9.2 $\text{Wm}^{-2}$, while the bias for full-sky LW is increased slightly from −1.1 to −2.2 $\text{Wm}^{-2}$, associated with the overestimate of the height of the thinnest cirrus clouds in the ISCCP results [*Chen and Rossow*, 2002]. The LW RMS differences and correlation coefficients are about the same, but the slope/intercepts of the scatterplots are significantly better, indicating a decrease of regional biases. However, the underestimate of $L\uparrow_t$ by FD in the subtropical dry regions is still the largest bias: reaching about a 10–12 $\text{Wm}^{-2}$. The FD $L\uparrow_t$ exceed the ERBE/CERES by almost

10 $Wm^{-2}$ over the high Greenland and Antarctic ice sheets. Except for CFC-$N_t$, which has a bias of $-7.3$ $Wm^{-2}$, all the other flux components have biases at or below 5 $Wm^{-2}$.

[57] The values shown in Table 6 are not globally complete but are averages of ISCCP-FD matched to ERBE. To obtain a better estimate for the global, annual means, we fill the unilluminated map grid cells in the polar regions with zeroes for SW in the ERBE data and reevaluate $N_t$ for the 4-year annual averages (based on four midseasonal months as done by *Rossow and Zhang* [1995]): The global, annual mean $N_t$ becomes +6.6 and +4.7 $Wm^{-2}$ for ERBE and FD, respectively. Our previous estimates of these two values were +4.8 and $-4.1$ $Wm^{-2}$ for ERBE and FC, respectively [cf. *Rossow and Zhang*, 1995, Table 2]. The slight difference between the two ERBE values is due to a change from using the ERBE daily-monthly mean to the hourly-monthly mean values (see footnotes to Table 6). Therefore the bias of the total net flux at TOA for the global annual mean has been reduced from about 9 to about 2 $Wm^{-2}$.

[58] We have also compared the ISCCP-FD fluxes with the ERBE-like monthly mean fluxes from CERES for 16 consecutive months from March 2000 to June 2001 when both data sets were available. As shown in the lower part of Table 6, the average and standard deviations of the differences are similar to (about 1 $Wm^{-2}$ "worse" than) those from the FD and ERBE comparison: The biases of $S\uparrow_t$ and CLR-$S\uparrow_t$ are 6.2 and 4.5 $Wm^{-2}$, respectively, and for $L\uparrow_t$ and CLR-$L\uparrow_t$, they are $-4.4$ and $-6.6$ $Wm^{-2}$, respectively. Since these CERES results are based on measurements from a single satellite in Sun-synchronous orbit, the required interpolations to account for angle and diurnal dependence are expected to be somewhat degraded from the original ERBE results. The CERES group has been working on new, more comprehensive angular distribution models (ADM) that will provide much more detailed scene type dependence that is being verified employing a second conically scanning instrument on each spacecraft [e.g., *Loeb et al.*, 2003]. Preliminary reports indicate that the direction of the improved ADMs is expected (in the global mean) to increase $S\uparrow_t$ and decrease $L\uparrow_t$ [*Loeb et al.*, 2002; *Loukachine et al.*, 2002] from the current ERBE-like results so both our SW and LW TOA flux biases may be further reduced when more accurate ADMs are implemented. Note that since FD and ERBE/CERES are completely independent data sources, their agreement to within their uncertainties should be a good validation for both.

[59] *Wielicki et al.* [2002] produced an anomaly time series of monthly mean TOA fluxes (with seasonal cycle removed) for 1985–1999, averaged over the tropical zone (20°S to 20°N), based on measurements from the single ERBE nonscanner instrument flying on the ERBS satellite. They interpreted this record as indicating a decadal variation in the tropical mean radiative energy budget that current climate models failed to simulate, even when forced with observed SSTs. We compare the flux anomalies from ISCCP-FD with a revised and altitude-corrected version of the ERBS data (obtained from B. A. Wielicki, 2004; both are relative to the 1985–1989 average). To improve the quantitative comparison, we linearly interpolate the FD monthly means to match ERBS 36-day-means (ten 36-day months per year) for the period from January 1985 to August 1999 (skipping the months that ERBS data are unavailable). Figures 6a, 6b, and 6c show their anomaly time series for $S\uparrow_t$, $L\uparrow_t$ and $N_t$, respectively. Given the estimated uncertainties of these two independent data sets (at least 3–5 $Wm^{-2}$ for ERBS and 5–10 $Wm^{-2}$ for ISCCP-FD), the agreement shown in the figures is surprisingly

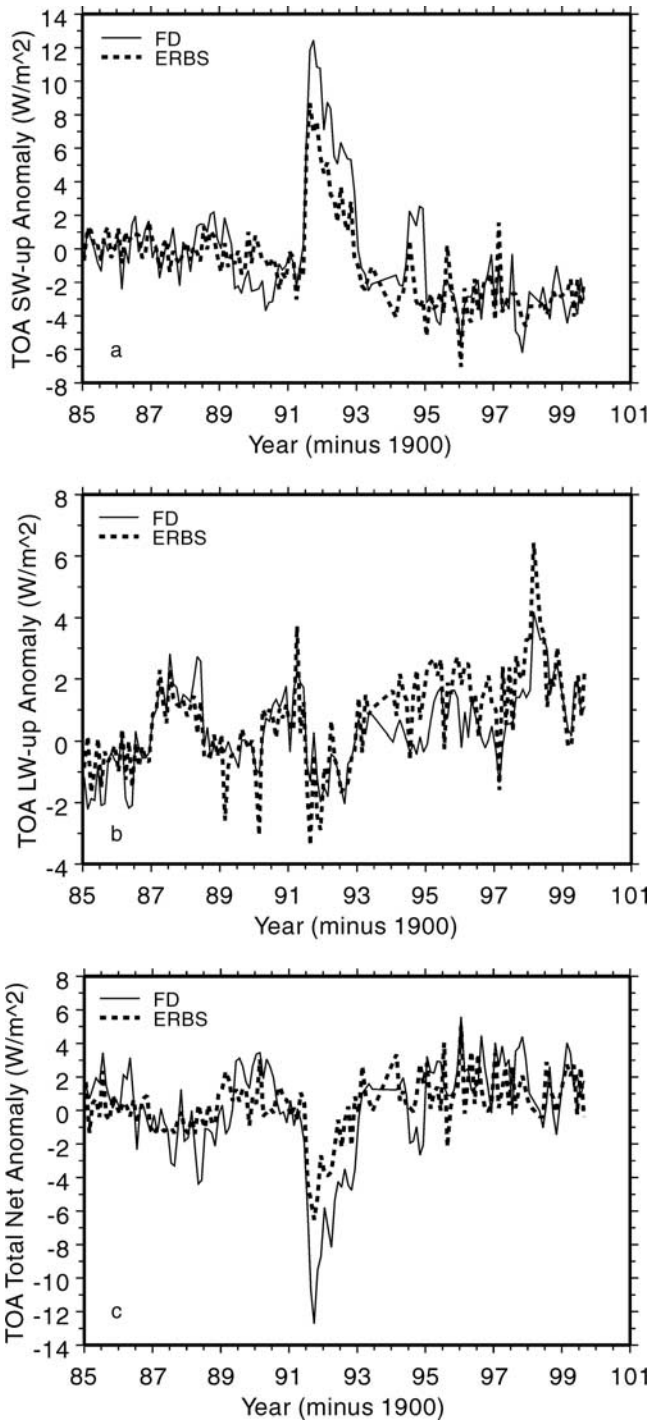


**Figure 6.** TOA flux anomaly time series for ISCCP-FD and ERBS for (a) $S\uparrow_t$, (b) $L\uparrow_t$ and (c) $N_t$. Values are 36-day averages for the zone, 20°S to 20°N, with mean seasonal cycle removed and the average for 1985–1989 set to zero. See comparison statistics in Table 7.

**Table 7.** Comparison Statistics for the 36-Day Monthly Mean (10 Months Per Year) Anomaly Time Series Between ISCCP-FD and ERBS[a]

| Quantity, W/m$^2$ | FD | ERBS | Mean Difference | Standard Deviation | Corr. Coeff., unitless | Slope, unitless | Intercept | Norm. Dev. |
|---|---|---|---|---|---|---|---|---|
| *All the Available 36-Day Months From Jan. 1985 to Aug. 1999 (Skipping No-Data Months)* | | | | | | | | |
| $S\uparrow_t$ | −0.37 | −0.84 | 0.477 | 1.868 | 0.8510 | 0.62 | −0.61 | 1.13 |
| $L\uparrow_t$ | 0.36 | 0.64 | −0.283 | 1.026 | 0.7469 | 0.89 | 0.32 | 0.76 |
| $N_t$ | 0.03 | 0.25 | −0.218 | 2.187 | 0.7261 | 0.42 | 0.24 | 1.13 |
| *Consecutive Eighty 36-Day Months From Jan. 1985 to Dec. 1992* | | | | | | | | |
| $S\uparrow_t$ | 1.08 | 0.57 | 0.525 | 1.926 | 0.8901 | 0.54 | −0.02 | 0.88 |
| $L\uparrow_t$ | −0.02 | −0.14 | 0.111 | 0.867 | 0.7694 | 0.72 | −0.12 | 0.64 |
| $N_t$ | −1.07 | −0.43 | −0.639 | 2.257 | 0.7965 | 0.41 | .00 | 0.97 |

[a]The upper part of the table is for the months from January 1985 to August 1999 (skipping all the months when ERBS has no data). The lower part of the table is for the 80 consecutive months from January 1985 to December 1992. ISCCP−FD 36-day-means are interpolated from their original normal monthly means (i.e., 12 months per year) to match ERBS 36-day monthly means (in total, 139 and 137 months for SW/NET and LW, respectively). Regression statistics are for ISCCP-FD and ERBS as $x$ and $y$, respectively.

good. The statistical comparison is shown in Table 7. The correlation coefficients between ISCCP-FD and ERBS are very high: 0.85, 0.75 and 0.73 for $S\uparrow_t$, $L\uparrow_t$ and $N_t$, respectively. The mean (RMS) differences (FD – ERBS) are 0.48 (1.9) Wm$^{-2}$ and −0.28 (1.0) Wm$^{-2}$ for $S\uparrow_t$ and $L\uparrow_t$, respectively. We will not examine the causes of agreement and discrepancy in this paper since much more investigation is required and is ongoing. *Chen et al.* [2002] have already noted that the SW anomalies might be explained by the ISCCP-observed changes in tropical total cloud cover and the LW anomalies by changes in both clouds and upper tropospheric water vapor amount. The good quantitative agreement shown in Figure 6 and Table 7 confirms these suggestions.

[60] The main SW anomalies also include a significant increase of about 12 (9) Wm$^{-2}$ for ISCCP-FD (ERBS) values of $S\uparrow_t$ right after the 1991 Mount Pinatubo eruption. The agreement for the Pinatubo anomaly is produced by explicitly including the variations of stratospheric aerosol [*Hansen et al.*, 2002, Figure 3] in our calculation, but the effect of the extra stratospheric aerosol is also aliased into the ISCCP cloud properties [cf. *Luo et al.*, 2002], which explains our overestimate relative to ERBE. The main LW anomalies of ERBS are generally also found in the ISCCP-FD values, but the amplitudes are generally smaller; for example, the maximum ERBS LW anomaly is about 6.5 Wm$^{-2}$ during the 1997/1998 El Niño and only 4+ Wm$^{-2}$ for ISCCP-FD.

### 5.2. Comparison With Surface Flux Measurements

[61] The effects of differences in space-time sampling between satellite-derived and surface-based measurements are even larger than for the satellite-to-satellite comparisons [*Rossow and Zhang*, 1995]. Like the ISCCP-FC data, the ISCCP-FD surface fluxes are calculated for 280 km equal-area cells, each of which has 50−100 (satellite pixel) samples (the DX pixels are 4−7 km in size but spatially sampled at 30 km intervals) that cover only about 3−5% of a grid cell's area. A more appropriate comparison between cell-mean FD and point surface values is obtained by using temporal averages so that the errors caused by the poor spatial match are somewhat reduced. For this reason, we focus on monthly mean comparisons between the FD and the surface data. Even for the higher spatial "resolution" of the ISCCP-FDX, the spatial matching does not necessarily improve since the all-sky hemispheric view of the surface instruments includes three-dimensional effects and covers a region of about 30−50 km in size compared with an DX pixel of a few kilometers. Moreover, some of the input parameters for FDX calculations are still based on 280 km equal-area cells (e.g., temperature and humidity profiles at 280 km) or even larger regions (e.g., the aerosol climatology at 5° × 4° longitude-latitude). In addition, the spectral range to which typical surface radiometers are sensitive is usually for wavelengths of 0.3 to 2.8 μm and 4.0 to 50 μm for SW and LW, respectively, which is not the same as our ranges of 0.2 to 5.0 μm and 5.0 to 200.0 μm, respectively. Such spectral differences may cause flux differences 1% [*Rossow and Zhang*, 1995].

[62] In our previous surface evaluation studies [*Rossow and Zhang*, 1995, Table 9], we compared monthly mean $S\downarrow_s$ and $L\downarrow_s$ from FC with all of the then-available surface measurements from the GEBA database [*Ohmura and Gilgen*, 1991]. GEBA collected $S\downarrow_s$ and $L\downarrow_s$ measurements for up to 5 years from about 2000 stations over the world. The estimated accuracy of the GEBA measurements is ±15 Wm$^{-2}$ for SW and ±10−30 Wm$^{-2}$ for LW [*Ohmura and Gilgen*, 1992]. We have redone the comparison with GEBA using the ISCCP-FD for the 2656 SW and 62 LW flux samples (the same as done for FC). The new comparison shows that the mean (RMS) differences (FD − GEBA) have decreased to 8.8 (21.5) from 15.2 (23.7) Wm$^{-2}$ for $S\downarrow_s$ and to −14.9 (17.9) from −19.4 (20.8) Wm$^{-2}$ for $L\downarrow_s$. Note that the sampling size for LW is too small to have real statistical significance.

[63] In October 1988, the World Meteorological Organization/International Council of Scientific Union (WMO/ICSU) Joint Scientific Committee (JSC) for World Climate Research Programme (WCRP) established BSRN to support climate research [*Ohmura et al.*, 1998]. The BSRN started operations in 1992 with 9 stations and has 35 sites currently. The original target accuracies for BSRN were ±5 Wm$^{-2}$ for $S\downarrow_s$ and ±20 Wm$^{-2}$ for $L\downarrow_s$, but significant improvements in procedures, instrument calibration and knowledge have led to estimated accuracies of ±5 Wm$^{-2}$ for $S\downarrow_s$ and ±10 Wm$^{-2}$ for $L\downarrow_s$ [*Ohmura et al.*, 1998].

[64] Table 8 summarizes the statistics of the comparison of all the available matched, monthly mean FD and BSRN values, totaling 1970 and 1831 data points for $S\downarrow_s$ and $L\downarrow_s$, respectively. For $S\downarrow_s$, the mean (RMS) difference (FD −

**Table 8.** Statistical Comparison Between ISCCP-FD and BSRN Monthly Means for 1992–2001[a]

| | FD | BSRN | Mean Difference | Stdv | Corr. Coef. | Slope | Intercept | Norm. Dev. | Sample No. |
|---|---|---|---|---|---|---|---|---|---|
| *Surface Downwelling SW and LW Fluxes for All ISCCP-FD and BSRN Data* | | | | | | | | | |
| $S\downarrow_s$ | 168.20 | 166.19 | 2.017 | 18.491 | 0.9825 | 0.96 | 3.90 | 13.07 | 1970 |
| $L\downarrow_s$ | 302.23 | 300.01 | 2.219 | 19.042 | 0.9706 | 1.05 | −17.40 | 12.89 | 1831 |
| *Surface Downwelling SW From ISCCP-FD and BSRN Separated Into Latitudinal Zones* | | | | | | | | | |
| 90°S to 65°S | 114.23 | 122.36 | −8.133 | 20.599 | 0.9907 | 1.05 | 2.31 | 13.38 | 302 |
| 65°S to 35°S | 145.18 | 165.15 | −19.972 | 15.370 | 0.9822 | 1.03 | 15.08 | 10.53 | 23 |
| 35°S to 15°S | 217.11 | 219.53 | −2.412 | 11.728 | 0.9847 | 1.00 | 2.32 | 8.29 | 144 |
| 15°S to 15°N | 247.72 | 226.40 | 21.318 | 13.963 | 0.8928 | 0.95 | −9.03 | 10.07 | 218 |
| 15°N to 35°N | 210.87 | 200.61 | 10.262 | 16.092 | 0.9742 | 0.97 | −4.65 | 11.45 | 243 |
| 35°N to 65°N | 168.34 | 168.23 | 0.116 | 14.180 | 0.9847 | 0.95 | 7.96 | 9.88 | 819 |
| 65°N to 90°N | 86.64 | 86.63 | 0.005 | 21.798 | 0.9724 | 0.97 | 3.01 | 15.51 | 221 |
| *Surface Downwelling LW Between ISCCP-FD and BSRN Separated Into Latitudinal Zones* | | | | | | | | | |
| 90°S to 65°S | 194.11 | 184.12 | 9.994 | 19.127 | 0.9478 | 1.14 | −36.49 | 11.90 | 276 |
| 65°S to 35°S | 316.67 | 297.85 | 18.820 | 17.132 | 0.2916 | 0.60 | 107.75 | 14.40 | 23 |
| 35°S to 15°S | 357.99 | 360.82 | −2.828 | 22.663 | 0.8122 | 1.09 | −30.75 | 15.18 | 141 |
| 15°S to 15°N | 414.65 | 415.33 | −0.680 | 8.797 | 0.8094 | 0.80 | 84.20 | 6.49 | 136 |
| 15°N to 35°N | 360.45 | 356.36 | 4.096 | 19.956 | 0.8634 | 1.00 | −4.25 | 14.11 | 237 |
| 35°N to 65°N | 305.72 | 307.05 | −1.327 | 17.688 | 0.9209 | 0.98 | 7.50 | 12.62 | 814 |
| 65°N to 90°N | 251.83 | 244.61 | 7.217 | 20.080 | 0.9293 | 1.33 | −91.49 | 10.18 | 204 |

[a]Difference is FD minus BSRN. All quantities are in W/m$^{-2}$, except the correlation coefficients, slopes and sample number. Regression statistics are for ISCCP-FD and BSRN as $x$ and $y$, respectively.

BSRN) is 2.0 (18.5) Wm$^{-2}$ and the correlation coefficient between the two sets is 0.98. For $L\downarrow_s$, these statistics become 2.2 (19.0) Wm$^{-2}$ and 0.97, respectively. Figure 7 shows the scatterplots for $S\downarrow_s$ and $L\downarrow_s$ (statistics in the top part of Table 8). The agreement between FD and BSRN is better than with GEBA for both the SW and LW, consistent with the higher quality expected of the BSRN data.

[65] To reveal the latitudinal behavior in the comparisons, the middle and bottom parts of Table 8 show the same comparison statistics for seven separate latitudinal zones. For the SW, most zones exhibit differences $\leq$10 Wm$^{-2}$; the largest mean differences appear in the tropical zone (21.3 Wm$^{-2}$), where biomass burning aerosol effects have not been (completely) accounted for in our calculations, and at southern high latitudes (−20.0 Wm$^{-2}$), where the sample size at the surface is very small (23). The largest RMS differences appear in the southern and northern polar regions (20.6 and 21.8 Wm$^{-2}$, respectively) with the rest of the zones exhibiting values $\leq$16 Wm$^{-2}$, which is consistent with the estimated cloud sampling effects [*Rossow and Zhang*, 1995]. The correlation coefficients in all zones are above 0.97 except in the tropical zone (0.89). For the LW, all the zones have mean differences $\leq$10 Wm$^{-2}$, except at southern high latitudes (18.8 Wm$^{-2}$) where the sample size is very small. Generally, the LW flux RMS differences are slightly larger than for the SW and the correlation coefficients are lower, but still $\geq$0.81, except again at southern high latitudes.

[66] We have also redone all the other surface flux case study comparisons for ISCCP-FDX that were done for ISCCP-FCX by *Rossow and Zhang* [1995]. For the first ISCCP Regional Experiment/Surface Radiation Budget (FIRE/SRB) 1986 [*Whitlock et al.*, 1990a, 1990b], the new results seem worse than previously for both $S\downarrow_s$ and $L\downarrow_s$, all the mean differences (FD minus observed) have become larger by 5–7 Wm$^{-2}$, even though the changes from ISCCP-FC to FD are consistent with the overall flux changes (decrease of $S\downarrow_s$ and $L\downarrow_s$). Nevertheless, the FD results are still within the range of the estimated uncertainties for the surface fluxes from this experiment. For the Tropical Ocean-Global Atmosphere Program–Coupled Ocean-Atmosphere Response Experiment (TOGA-COARE) pilot cruise 1990 [*Young et al.*, 1992], the biases in $S\downarrow_s$ and $L\downarrow_s$ are reduced by 6–9 Wm$^{-2}$ (by 2–3 Wm$^{-2}$ for $L\uparrow_s$). All other statistics are changed only slightly.

[67] Beginning in 1999, the SeaFlux project [*Curry et al.*, 2004] has been working to promote improved theories and methods for calculating accurate, high-time-resolution surface turbulent fluxes for ocean model surface forcing. We have participated in the project by providing surface radiative fluxes (ISCCP-FDX) for all ISCCP-DX pixels within an (280 km) equal-area box centered on a moving or stationary ship location. All of the ships have radiometers measuring radiative fluxes that offer an opportunity to evaluate our fluxes. In this case, we compare the fluxes from the DX pixel nearest to the ship with the direct measurements on the ships. There are 20 available cruises (amounting to over 300 months of hourly flux measurements), covering the tropics, subtropics, midlatitudes and the north polar oceans, that are used for this comparison as contrasted with only four cases in our 1995 work. For the majority of the SeaFlux cases, the bias (FDX - measured) is <10 Wm$^{-2}$ for $S\downarrow_s$; the average bias (RMS difference) over all the cases is +5.8 (22.7) Wm$^{-2}$. The correlation coefficients are > 0.9 for almost all cases with an average of 0.96. For $L\downarrow_s$, the bias (RMS difference) over all the cases is −0.8 (18.6) Wm$^{-2}$, but the average correlation coefficient is only 0.56. For comparisons of hourly mean results, RMS differences are 102.6 Wm$^{-2}$ for $S\downarrow_s$ and 28.7 Wm$^{-2}$ for $L\downarrow_s$. Although the average FDX flux differences are generally improvements compared with FCX fluxes, the persistent large RMS differences for small-scale comparisons of $S\downarrow_s$ are caused by differing sampling of the cloud variations and for $L\downarrow_s$, especially at lower latitudes, by spuriously large variability in the TOVS atmospheric temperature compared to surface measurements, probably due to measurement

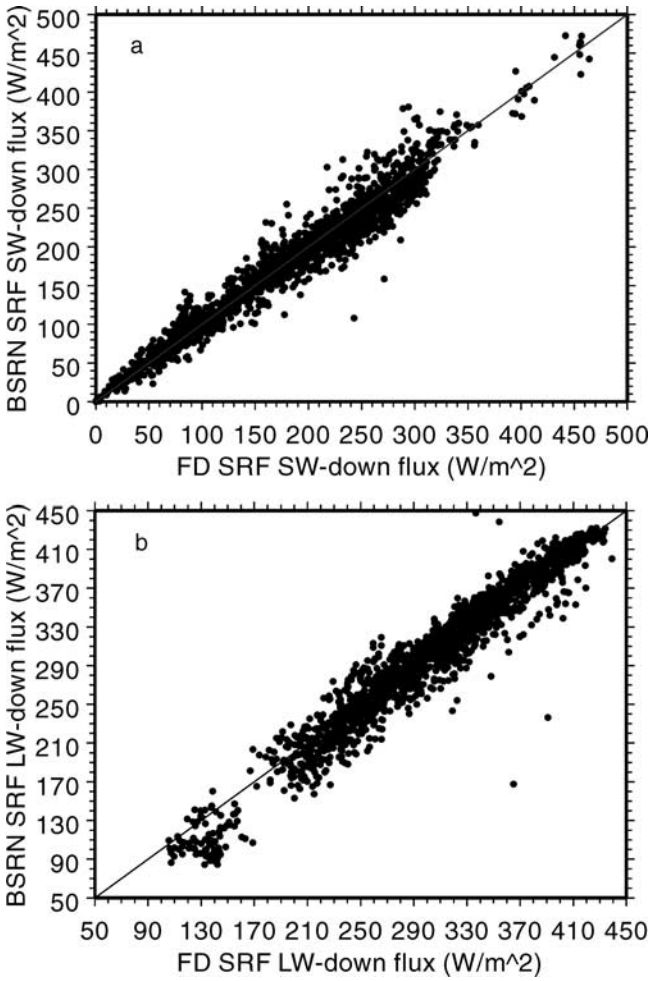


**Figure 7.** Scatterplots for all the available monthly mean surface fluxes from BSRN and corresponding values from ISCCP-FD: (a) $S\downarrow_s$ and (b) $L\downarrow_s$ in $Wm^{-2}$. Statistics from the plot are given in the top part of Table 8.

errors. For example, the SeaFlux data collection [*Curry et al.*, 2004] shows that at low latitudes, the standard deviation of $T_a$ values from TOVS is 2–3 K, about twice the standard deviation measured from surface ships (see also discussion by *Rossow and Zhang* [1995]).

## 6. Summary and Discussion

### 6.1. Summary of Improvements

[68] Some of the largest improvements of ISCCP-FD relative to ISCCP-FC, as confirmed by comparisons to more direct measurements at TOA and the surface, are attributable to improvements of the ISCCP D-series data [cf. *Rossow and Schiffer*, 1999]. Not only is the global high bias of $S\uparrow_t$ reduced, but also larger regional overestimates of $S\uparrow_t$ are significantly reduced in areas where high-level ice clouds predominate. Table 3 shows that $S\uparrow_t$ reduction by the ice cloud treatment is composed of reductions by decreased optical thicknesses in the ISCCP retrieval and the reduced reflectivity of larger particle sizes, offset by the increased reflectivity of nonspherical particles. Accounting for cloud type mixtures and mesoscale inhomogeneity also reduces cloud reflectivity generally. However, relative to ERBE, marine boundary layer clouds are too reflective. About one half of the overall reduction of $S\uparrow_t$ is caused by the combined effects of the increased spectral resolution of the radiation model, which increases atmospheric absorption and generally reduces land surface albedos, the aerosol correction of the ISCCP land $R_s$ values, and the improved ocean albedo model.

[69] The ice cloud treatment, together with an increased detection of thin cirrus over land, produced a decrease of the global mean $L\uparrow_t$ of almost 3 $Wm^{-2}$ (Table 3) and significantly decreased larger regional discrepancies, but the small effects of the thinnest cirrus have been exaggerated somewhat [cf. *Chen and Rossow*, 2002]. An increase of $L\uparrow_t$ caused by the treatment of cloud type mixtures is nearly offset by a decrease associated with introducing the cloud vertical structure model. The increased spectral resolution of the radiative transfer model increased $L\uparrow_t$ by about 3 $Wm^{-2}$, but this was offset by the improved upper troposphere, lower stratosphere properties from SAGE and TOMS.

[70] The improved cloud detection over land reduced cloud contamination effects on $T_s$, reducing some significant regional low biases of $L\uparrow_s$. The other cloud-related improvement in surface LW fluxes comes from the introduction of the cloud vertical structure model, which has the effect of increasing the average cloud base pressure (compare Figure 4c) and decreasing the bias of $L\downarrow_s$. However, the original estimate of the $L\downarrow_s$ bias was based only on the very small sample from GEBA, so it was highly uncertain. The current LW agreement with the BSRN data is very good. Significant errors in the ISCCP-FC LW fluxes at the surface were also produced by neglecting the diurnal variations of $T_a$, including the sampling bias of the TOVS data together with some errors in extrapolating the TOVS profiles to the surface, and by neglecting the cloud radiative effects on the diurnal variations of $T_s$ (Table 3). Correcting these deficiencies reduced the bias in ISCCP-FD. The remainder of the bias reduction in $L\downarrow_s$ comes from changes in the radiative transfer model spectral resolution and water vapor continuum absorption. Despite the successful reduction of bias (compared with BSRN measurements), the uncertainty of $L\downarrow_s$ remains large because of the uncertainties of TOVS atmospheric temperature measurements.

[71] Although the low bias in $L\uparrow_t$ in the subtropics has been reduced by modifying the vertical distribution (but not the total abundance) of water vapor (see AM, 2003JD004457-IO.txt), this problem still accounts for the largest systematic (regional) disagreement with ERBE/CERES, reaching 10–12 $Wm^{-2}$ in some locations.

[72] The aerosol climatology employed in the ISCCP-FD product is "state-of-the-art" and certainly less biased than the one used in the ISCCP-FC products. Although the uncertainties of aerosol abundance and optical properties are still large, the effect of these uncertainties on the average fluxes is small (as judged by comparisons with ERBE/CERES and BSRN). The most important effect of the aerosol changes was to increase the atmospheric SW absorption by an amount that is a little larger than the total effect of the ice cloud microphysical changes (Table 3), which allowed for both $S\uparrow_t$ and $S\downarrow_s$ to be improved. The largest remaining error is caused by episodic and regional biomass burning events [*Levine*, 1996], which are frequent

in the tropics, where the comparison with BSRN sites shows a persistent ≈20 $Wm^{-2}$ high bias in the FD values of $S\downarrow_s$. Note however, that the largest of these events are probably detected as clouds in the ISCCP data set, so that their effect on the fluxes is partially captured.

[73] The new feature of the ISCCP-FD data set is that it contains fluxes at five levels providing the whole atmospheric vertical flux profile (PRF), TOA and SRF inclusive. The PRF improve the diagnostic usefulness of this data set by providing more detail about the vertical distribution of radiative heating/cooling in the atmosphere and how clouds affect it. We have already shown that the TOA and SRF fluxes are not very sensitive to variations in the vertical cloud structure (the most uncertain component) [*Zhang et al.*, 1995; *Chen et al.*, 2000], but we now retain explicit information about the vertical structure, which underlies the calculations, to diagnose more completely the cloud-radiative effects.

### 6.2. Summary of Remaining Uncertainties

[74] All of previous sensitivity tests were repeated, along with new ones for new features, to document the uncertainty of the calculated fluxes associated with the uncertainties of the input variables. Most of these uncertainties are summarized in AM, 2003JD004457-MODEL.txt. Comparing the ISCCP-FD fluxes with the same direct measurements as the ISCCP-FC fluxes shows general improvement. Almost all the monthly, global mean flux biases (regional RMS differences) at TOA (FD − ERBE) have decreased in magnitude (Table 6): +4.7 (6) and +0.9 (8) $Wm^{-2}$ for $S\uparrow_t$ and CLR-$S\uparrow_t$, respectively, compared with +10.7 (7) and +4.1 (8) $Wm^{-2}$ for FC, and −2.2 (3) and −5.6 (4) $Wm^{-2}$ for $L\uparrow_t$ and CLR-$L\uparrow_t$, respectively, compared with −1.1 (4) and −9.2 (4) $Wm^{-2}$ for FC. Except for CFC-$N_t$, which has a bias of −7.3 $Wm^{-2}$, all the other flux components have biases at or below 5 $Wm^{-2}$. The global mean, total net fluxes, averaged over 4 years (based on the four midseason months), are +6.6 and +4.7 $Wm^{-2}$ for ERBE and FD, respectively. (When averaged over a globally full map, the global mean of the calculated total net flux at TOA has changed to about +3 $Wm^{-2}$ from about −4.) Likewise, all the monthly mean flux biases (site-to-site RMS differences) at the surface (FD − GEBA) have decreased: +8.8 (15) $Wm^{-2}$ for $S\downarrow_s$, compared with +15.2 (16) $Wm^{-2}$ for FC, and −14.9 (13) $Wm^{-2}$ for $L\downarrow_s$, compared with −19.4 (13) $Wm^{-2}$ for FC. The comparisons between FD and the better quality BSRN surface fluxes suggest even smaller biases (top part of Table 8): +2.0 (13) $Wm^{-2}$ for $S\downarrow_s$ and +2.2 (13) $Wm^{-2}$ for $L\downarrow_s$, but there are still some larger regional biases (middle and bottom parts of Table 8), especially for SW fluxes in the tropics. The RMS differences in monthly mean values are indicative of the larger regional uncertainties in surface fluxes that remain because of aerosols for SW and atmospheric and surface temperatures for LW (based on the sensitivity tests and estimates of the uncertainties of the input data [cf. *Zhang et al.*, 1995].

[75] In summary, our FC fluxes had overall uncertainties at TOA of 10–15 $Wm^{-2}$ and at the surface of 20–25 $Wm^{-2}$ for regional and monthly means, where much of the uncertainty in SW fluxes was bias and much of the uncertainty in LW fluxes was more random. The new FD fluxes appear to have biases that are <10 $Wm^{-2}$ (possibly even ≈5 $Wm^{-2}$) and regional RMS differences that are somewhat smaller than before. Nevertheless, the overall uncertainty of these fluxes remains at least 5–10 $Wm^{-2}$ at TOA and 10–15 $Wm^{-2}$ at the surface. For instantaneous fluxes, the largest sources of uncertainty are caused by sparse sampling of cloud variations by ISCCP for $S\uparrow_t$ and $S\downarrow_s$, by measurement errors in TOVS atmospheric temperatures for $L\downarrow_s$, by measurement errors in ISCCP surface temperatures for $L\uparrow_s$, and by errors in water vapor vertical profiles where high-level clouds are rare for $L\uparrow_t$.

[76] Some of the persistent regional biases in our TOA fluxes, compared with ERBE, are associated with particular cloud types: For $S\uparrow_t$ there are 10–12 $Wm^{-2}$ high biases for marine stratus and 5–7 $Wm^{-2}$ low biases in the ITCZ (there are also still significant differences as large as +10–20 $Wm^{-2}$ at some land locations and as large as −10–20 $Wm^{-2}$ over the ice sheets for CLR-$S\uparrow_t$). For $L\uparrow_t$ there are still 4–8 $Wm^{-2}$ high biases in the ITCZ [cf. *Chen and Rossow*, 2002]. However, the accuracy of the ERBE ADMs for specific cloud types, especially ones that are very different from global mean conditions, is uncertain, so further evaluation of cloud-type dependence must await the improved CERES ADMs.

[77] Currently, the uncertainty of the global distribution of flux profiles is virtually impossible to assess since there are no other comprehensive PRF measurements. *Chen et al.* [2000] considered the sensitivity of the net flux profiles to varying assumptions about cloud layer overlap and showed that the (4-day) average atmospheric radiative heating rate (net flux) uncertainty is not too large when compared with the total radiative heating, but that the instantaneous uncertainty in the net fluxes is comparable to the total cloud effect on the radiative heating. In general, even with our cloud vertical structure (CVS) model, the amount of low-level cloud is probably underestimated (Rossow et al., submitted manuscript, 2004). Consequently, the heating (due to absorbed SW) would be slightly shifted to higher altitudes from lower altitudes and the total atmospheric heating reduced slightly by preventing sunlight from reaching the water vapor near the surface. The errors in LW heating rate profiles are smaller in the moister parts of the atmosphere, but very important in the colder, drier parts; hence errors in our CVS are likely to be more important at higher latitudes.

[78] A key issue in evaluating the PRF results and the importance of cloud effects on radiative heating is whether the proper correlation of the cloud-induced radiative heating perturbations with the meteorology has been captured. We note that the studies of *Lau and Crane* [1995, 1997], *Machado and Rossow* [1993] and *Tselioudis et al.* [2000] have shown that the ISCCP cloud types appear in the expected locations and with the expected relationships to particular meteorological events. The assumed connection between these types and the cloud vertical structure that we use therefore provides a reasonable correlation with meteorology (see Rossow et al., submitted manuscript, 2004). Evaluation of the accuracy of these results will require more work with the long-term records now becoming available from radar/lidar measurements at the Atmospheric Radiation Measurement (ARM) [*Ackerman and Stokes*, 2003] sites and by comparison with results from the CloudSat

**Table 9.** Global Average Monthly Means for the Four Seasonal Months (January, April, July, and October), (Pseudo) Annual Mean Based on the Four Seasonal Months From April 1985 to January 1989, and Annual Mean Based on 12 Months for 5 Years (1985–1989)

| | 1986–1989 Jan. | 1985–1988 April | 1985–1988 July | 1985–1988 Oct. | Pseudo ANN[a] | 5-Year, 12-Month ANN |
|---|---|---|---|---|---|---|
| $S\downarrow_t$ | 352.97 | 339.28 | 330.96 | 344.03 | 341.81 | 341.82 |
| $S\uparrow_t$ | 112.07 | 104.55 | 99.80 | 105.87 | 105.57 | 105.71 |
| $S\downarrow_s$ | 195.50 | 190.84 | 179.96 | 191.42 | 189.43 | 189.21 |
| $S\uparrow_s$ | 26.08 | 26.16 | 20.03 | 23.79 | 24.01 | 24.02 |
| $L\downarrow_t$ | 0.00 | 0.00 | 0.00 | 0.00 | 0.00 | 0.00 |
| $L\uparrow_t$ | 231.33 | 231.86 | 236.04 | 233.29 | 233.13 | 233.29 |
| $L\downarrow_s$ | 337.47 | 342.97 | 353.13 | 344.58 | 344.54 | 344.65 |
| $L\uparrow_s$ | 386.95 | 397.91 | 402.28 | 395.56 | 395.67 | 395.58 |
| CLR-$S\downarrow_t$ | 352.97 | 339.28 | 330.96 | 344.03 | 341.81 | 341.82 |
| CLR-$S\uparrow_t$ | 56.48 | 57.62 | 52.12 | 54.59 | 55.20 | 55.36 |
| CLR-$S\downarrow_s$ | 260.32 | 246.81 | 235.28 | 251.06 | 248.37 | 248.26 |
| CLR-$S\uparrow_s$ | 32.01 | 32.60 | 25.12 | 29.03 | 29.69 | 29.82 |
| CLR-$L\downarrow_t$ | .00 | .00 | .00 | .00 | .00 | .00 |
| CLR-$L\uparrow_t$ | 257.31 | 259.42 | 261.79 | 258.87 | 259.35 | 259.48 |
| CLR-$L\downarrow_s$ | 304.62 | 312.70 | 323.96 | 313.76 | 313.76 | 313.54 |
| CLR-$L\uparrow_s$ | 385.35 | 396.44 | 400.88 | 394.08 | 394.19 | 394.08 |
| CLD-$S\downarrow_t$ | 352.97 | 339.28 | 330.96 | 344.03 | 341.81 | 341.82 |
| CLD-$S\uparrow_t$ | 126.68 | 117.35 | 113.84 | 119.47 | 119.33 | 119.52 |
| CLD-$S\downarrow_s$ | 176.71 | 174.52 | 163.02 | 175.01 | 172.32 | 172.01 |
| CLD-$S\uparrow_s$ | 23.33 | 23.79 | 18.20 | 22.13 | 21.86 | 21.84 |
| CLD-$L\downarrow_t$ | 0.00 | 0.00 | 0.00 | 0.00 | 0.00 | 0.00 |
| CLD-$L\uparrow_t$ | 225.34 | 224.98 | 229.23 | 226.88 | 226.61 | 226.80 |
| CLD-$L\downarrow_s$ | 352.53 | 356.62 | 367.31 | 358.53 | 358.75 | 358.97 |
| CLD-$L\uparrow_s$ | 387.67 | 398.57 | 402.96 | 396.23 | 396.36 | 396.27 |
| CFC-$S\downarrow_t$ | 0.00 | 0.00 | 0.00 | 0.00 | 0.00 | 0.00 |
| CFC-$S\uparrow_t$ | 55.59 | 46.93 | 47.68 | 51.27 | 50.37 | 50.34 |
| CFC-$S\downarrow_s$ | −64.82 | −55.98 | −55.32 | −59.64 | −58.94 | −59.05 |
| CFC-$S\uparrow_s$ | −5.92 | −6.44 | −5.09 | −5.24 | −5.68 | −5.80 |
| CFC-$L\downarrow_t$ | 0.00 | 0.00 | 0.00 | 0.00 | 0.00 | 0.00 |
| CFC-$L\uparrow_t$ | −25.97 | −27.56 | −25.75 | −25.58 | −26.22 | −26.19 |
| CFC-$L\downarrow_s$ | 32.84 | 30.27 | 29.17 | 30.82 | 30.78 | 31.11 |
| CFC-$L\uparrow_s$ | 1.60 | 1.47 | 1.40 | 1.48 | 1.49 | 1.50 |

[a]Compare *Rossow and Zhang* [1995].

[*Stephens et al.*, 2002] and Calipso [*Currey*, 2002] spacecraft missions, which are scheduled for launch in early 2005.

### 6.3. Mean Meridional Cross Section of Net Fluxes and Cloud Effects

[79] Tables 9 and 10 replace Tables 11 and 12 in the work of *Rossow and Zhang* [1995] showing the global, seasonal and annual mean values of the fluxes and net fluxes, respectively. In addition, the full 12-month annual mean values are also shown to compare with the 4-month annual means calculated before: Generally, these two ways of calculating the annual mean are the same within about 1 $Wm^{-2}$. This summary shows that our estimate of the global annual mean planetary (TOA) radiative balance is +2.8 $Wm^{-2}$ with a planetary albedo of 30.9% and effective emission temperature of 253.6 K. This imbalance is roughly consistent with estimates of the current radiative imbalance due to greenhouse gas and aerosol changes [*Hansen et al.*, 2002], which are included in these calculations, but the absolute uncertainty of this value is at least ±5–10 $Wm^{-2}$. The planetary albedo without clouds is 16.2% and the effective emission temperature without clouds is 260.5 K. The seasonal ranges of the global mean values of $NS_t$ and $NL_t$ are about 10 and 5 $Wm^{-2}$, respectively; the largest monthly imbalance is the heating in January, whereas in our 95 results, the largest imbalance was the cooling in July. Most (70%) of the planetary SW heating occurs at the surface whereas most (78%) of the LW cooling comes from the atmosphere. More SW absorption occurs in the lower tropical troposphere than at higher latitudes and more LW emission comes from the polar surface than at lower latitudes (see below). Because of the greenhouse effect, the net radiative balance at the surface is +114.2 $Wm^{-2}$, offset by evaporative cooling, and the net radiative balance of the atmosphere is −111.4 $Wm^{-2}$, offset by precipitation heating. The seasonal ranges of surface radiative heating and atmospheric radiative cooling are both about 10 $Wm^{-2}$, but the maximum (minimum) heating occurs at the surface in January (April) while the maximum (minimum) cooling in the atmosphere occurs in July (April). Compared with our 95 results, the atmospheric SW absorption has increased by about 5 $Wm^{-2}$ and the LW cooling of the atmosphere and surface has increased by about 5 $Wm^{-2}$.

[80] The global annual mean cloud flux changes (CFC = full-sky flux minus clear-sky flux) in Tables 9 and 10 are subtle: At TOA, clouds decrease the absorbed SW by 50.3 $Wm^{-2}$ and the emitted LW by 26.2 $Wm^{-2}$, producing a net planetary cooling of 24.2 $Wm^{-2}$. The SW CFC is slightly larger at the surface than at TOA because of additional atmospheric absorption due mostly to the correlated increase in water vapor with clouds that we include in our calculations. The LW CFC effect is also slightly larger at the surface than at TOA because the clouds, overall, provide a slight increase in the cooling efficiency of the atmosphere. These results reiterate the point that a near-cancellation of the cloud flux changes at TOA, which is mistakenly described as ''zero forcing,'' actually amounts to

**Table 10.** Global Average Monthly Means for the Four Seasonal Months (January, April, July, and October), (Pseudo) Annual Mean Based on the Four Seasonal Months from April 1985 to January 1989, and Annual Mean Based on 12 Months for 5 Years (1985–1989)

| | 1986–1989 Jan. | 1985–1988 April | 1985–1988 July | 1985–1988 Oct. | Pseudo ANN[a] | 5-Year, 12-Month ANN |
|---|---|---|---|---|---|---|
| $NS_t$ | 240.90 | 234.73 | 231.16 | 238.16 | 236.24 | 236.11 |
| $NS_s$ | 169.42 | 164.67 | 159.94 | 167.63 | 165.42 | 165.19 |
| $NS_a$ | 71.48 | 70.05 | 71.22 | 70.53 | 70.82 | 70.92 |
| $NL_t$ | −231.33 | −231.86 | −236.04 | −233.29 | −233.13 | −233.29 |
| $NL_s$ | −49.48 | −54.94 | −49.15 | −50.97 | −51.14 | −50.93 |
| $NL_a$ | −181.85 | −176.92 | −186.89 | −182.32 | −181.99 | −182.36 |
| $N_t$ | 9.57 | 2.87 | −4.88 | 4.87 | 3.11 | 2.82 |
| $N_s$ | 119.94 | 109.73 | 110.79 | 116.66 | 114.28 | 114.25 |
| $N_a$ | −110.37 | −106.87 | −115.67 | −111.79 | −111.17 | −111.44 |
| CLR-$NS_t$ | 296.49 | 281.66 | 278.84 | 289.44 | 286.61 | 286.46 |
| CLR-$NS_s$ | 228.31 | 214.21 | 210.16 | 222.03 | 218.68 | 218.44 |
| CLR-$NS_a$ | 68.18 | 67.45 | 68.68 | 67.40 | 67.93 | 68.01 |
| CLR-$NL_t$ | −257.31 | −259.42 | −261.79 | −258.87 | −259.35 | −259.48 |
| CLR-$NL_s$ | −80.72 | −83.74 | −76.92 | −80.32 | −80.42 | −80.54 |
| CLR-$NL_a$ | −176.58 | −175.68 | −184.88 | −178.55 | −178.92 | −178.94 |
| CLR-$N_t$ | 39.19 | 22.24 | 17.05 | 30.57 | 27.26 | 26.98 |
| CLR-$N_s$ | 147.59 | 130.47 | 133.24 | 141.71 | 138.25 | 137.90 |
| CLR-$N_a$ | −108.40 | −108.23 | −116.20 | −111.15 | −110.99 | −110.93 |
| CLD-$NS_t$ | 226.30 | 221.93 | 217.12 | 224.56 | 222.48 | 222.30 |
| CLD-$NS_s$ | 153.38 | 150.73 | 144.83 | 152.87 | 150.45 | 150.16 |
| CLD-$NS_a$ | 72.92 | 71.20 | 72.29 | 71.68 | 72.02 | 72.14 |
| CLD-$NL_t$ | −225.34 | −224.98 | −229.23 | −226.88 | −226.61 | −226.80 |
| CLD-$NL_s$ | −35.14 | −41.95 | −35.65 | −37.69 | −37.61 | −37.31 |
| CLD-$NL_a$ | −190.20 | −183.03 | −193.58 | −189.19 | −189.00 | −189.49 |
| CLD-$N_t$ | .96 | −3.06 | −12.10 | −2.33 | −4.13 | −4.50 |
| CLD-$N_s$ | 118.24 | 108.78 | 109.18 | 115.18 | 112.84 | 112.86 |
| CLD-$N_a$ | −117.28 | −111.83 | −121.28 | −117.51 | −116.98 | −117.36 |
| CFC-$NS_t$ | −55.59 | −46.93 | −47.68 | −51.27 | −50.37 | −50.34 |
| CFC-$NS_s$ | −58.89 | −49.54 | −50.22 | −54.40 | −53.26 | −53.25 |
| CFC-$NS_a$ | 3.30 | 2.60 | 2.54 | 3.13 | 2.89 | 2.91 |
| CFC-$NL_t$ | 25.97 | 27.56 | 25.75 | 25.58 | 26.22 | 26.19 |
| CFC-$NL_s$ | 31.24 | 28.80 | 27.77 | 29.35 | 29.29 | 29.61 |
| CFC-$NL_a$ | −5.27 | −1.24 | −2.01 | −3.77 | −3.07 | −3.42 |
| CFC-$N_t$ | −29.62 | −19.37 | −21.93 | −25.70 | −24.15 | −24.16 |
| CFC-$N_s$ | −27.65 | −20.74 | −22.46 | −25.05 | −23.97 | −23.65 |
| CFC-$N_a$ | −1.97 | 1.36 | .53 | −.64 | −.18 | −.51 |

[a]Compare *Rossow and Zhang* [1995].

a significant change in the vertical gradient of radiative heating because the SW and LW effects appear at the surface and in the atmosphere, respectively. Moreover, although the global mean CFC-$N_a$ is nearly zero, the clouds change both the vertical and horizontal gradients of the radiative heating within the atmosphere (see below), which alters the forcing of the atmospheric circulation.

[81] Table 11 illustrates the new feature of these calculations by showing the annual mean vertical net flux profiles for full sky and clear sky. The values indicate how much energy is gained or lost from below the particular pressure level. The CLR-NS shows that most of the SW flux is absorbed at the surface and in the lowest layer of the atmosphere where water vapor is most abundant. Clouds not only reduce the total absorbed SW (mostly at the surface) but also shift some of the atmospheric SW absorption, in a relative sense, into the upper troposphere above the 440 mbar level. The CLR-NL shows that only about one third of the total comes from the surface, the rest comes from the atmosphere. Clouds not only reduce the total emitted LW (mostly at the surface) but also shift some of the emission to higher altitudes, in a relative sense. Note that a bit more than 5% of the net fluxes occur in the stratosphere; this fraction is increased by the cloud effects.

[82] Figure 8 shows the annual mean pressure-latitude cross sections of CLR-NS, CLR-NL and CLR-$N$ (the values

**Table 11.** Global and Multiyear Annual Mean Fluxes at the Surface and TOA and in the Four Atmospheric Layers as Indicated for 1985–1989 From ISCCP-FD[a]

| Atmospheric Level/Layer | NS | NL | N | CLR-NS | CLR-NL | CLR-$N$ |
|---|---|---|---|---|---|---|
| TOA | 236.13 | −233.32 | 2.82 | 286.50 | −259.50 | 27.00 |
| 100 mbar to TOA | 13.72 | −17.98 | −4.25 | 12.53 | −17.01 | −4.49 |
| 440–100 mbar | 20.06 | −42.84 | −22.79 | 15.90 | −40.33 | −24.44 |
| 680–440 mbar | 15.48 | −46.70 | −31.22 | 15.61 | −44.63 | −29.03 |
| SRF to 680 mbar | 21.87 | −75.44 | −53.57 | 24.22 | −77.60 | −53.38 |
| Surface | 165.19 | −50.92 | 114.28 | 218.47 | −80.53 | 137.94 |

[a]Annual mean fluxes are given in $Wm^{-2}$.

indicate the amount of energy gained or lost below a particular pressure level, not the heating or cooling rate at a particular level). The dominant equator-to-pole decrease of CLR-NS (Figure 8a) is obvious; the nearly vertical contours also indicate the relative transparency of the atmosphere with the strongest absorption by water vapor in the lower tropical troposphere causing the largest deviations of the contours from vertical. On the other hand, the nearly horizontal contours of CLR-NL (Figure 8b) indicate the relatively opaque atmosphere and the effects of poleward heat transports by the ocean and atmosphere that produce a more uniform LW emission. Figure 8c shows CLR-*N* varying from a maximum at the equatorial surface to minima at the polar tropopause.

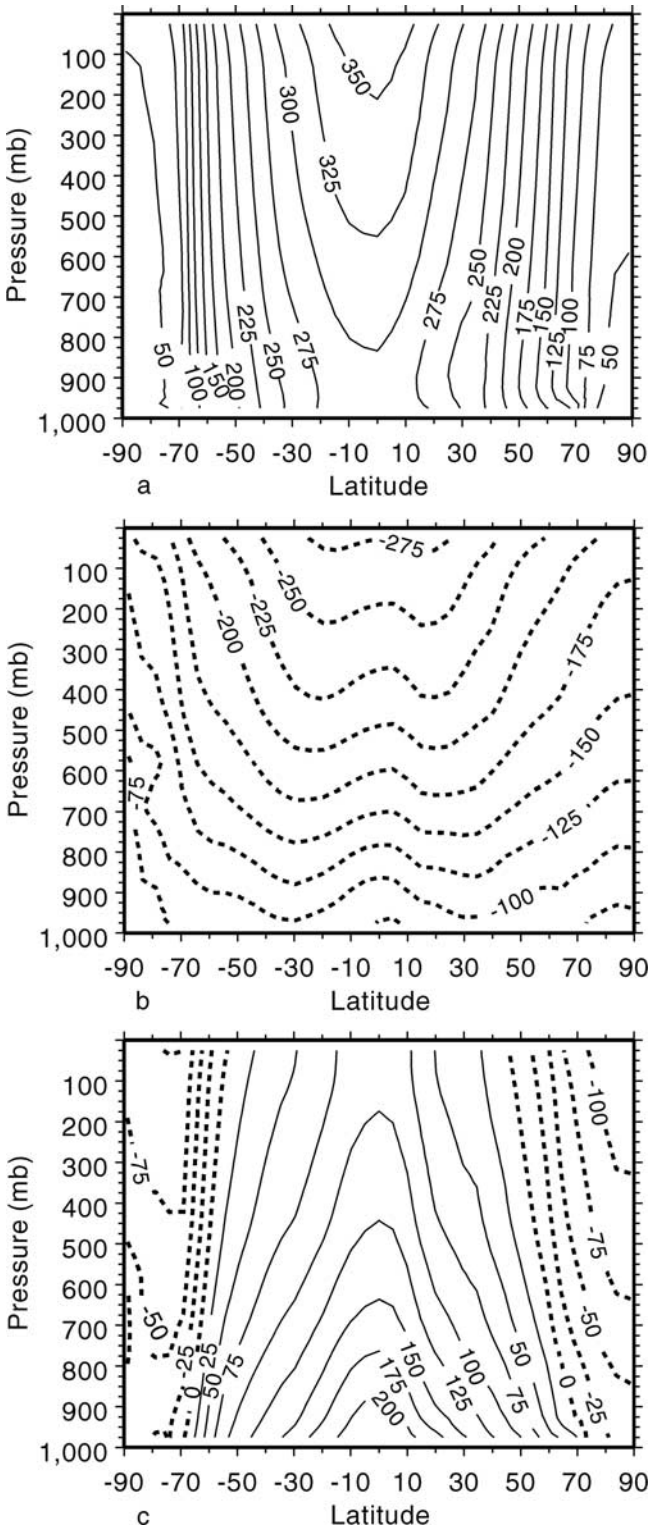


**Figure 8.** Mean pressure-latitude cross sections of clear-sky net fluxes in $Wm^{-2}$ (linearly interpolated from the original 5-level profiles) averaged over 1985–1989: (a) CLR-NS, (b) CLR-NL and (c) CLR-*N*. The sign convention indicates the energy gained (positive values, solid curves) or lost (negative values, dashed curves) below a given pressure level. Thus the net SW at the top is the total amount absorbed at that latitude by the atmosphere and surface, whereas the net SW at the bottom is the total amount absorbed at that latitude by the surface.

[83] The pattern for the full-sky net fluxes is very similar to that in Figure 8 because the cloud effects are relatively small, especially for SW. The net radiative flux pattern (similar to Figure 8c) is sometimes mistakenly referred to as the forcing for the climate, but it is in fact produced by combining the true forcing, $S\downarrow_t$, with part of the response (NL); in fact, both the observed NS and NL have been altered by the operation of water vapor and cloud feedbacks. So, the pattern in Figure 8c is what results after the climate has responded to the radiative forcing.

[84] In the work of *Rossow and Zhang* [1995] and *Zhang and Rossow* [1997], we illustrated the cloud effects on the mean meridional heat transports of the atmosphere and ocean: The cloud effects on the horizontal gradients of the radiative heating were such as to reduce the strength of the oceanic circulation (mostly SW) and enhance the atmospheric circulation (mostly LW). Figure 9 shows the annual mean pressure-latitude cross sections of CFC-NS, CFC-NL and CFC-*N*, adding the vertical dimension to our previous discussion (when the values in Figure 9 are added to the values in Figure 8, the full-sky net fluxes are obtained). The clouds generally reduce NS (all negative values in Figure 9a), most notably in the midlatitude and tropical storm zones. The generally vertical contours indicate that they do not make much change in the SW absorbed by the atmosphere: Small maxima in the midlatitude and tropical storm zones indicate a small upward shift of the SW heating (compare Table 11). The SW heating of the atmosphere and the cloud effects on it are weak. The more important cloud effects are the larger ones on NL (Figure 9b), where the positive values indicate decreased cooling (an effective heating). The fact that the contours are not vertical indicates that the clouds alter the vertical gradients in LW cooling, producing a high-level heat source in the tropics that suppresses convection [cf. *Rind and Rossow*, 1984; *Wang and Rossow*, 1998]. The cloud effect on the horizontal LW cooling gradient enhances the mean Hadley circulation [cf. *Rossow and Zhang*, 1995], but the feedback between these radiative effects on convection and the large-scale circulation can produce more complicated responses [*Rind and Rossow*, 1984]. The cloud effects at higher latitudes are more complicated because they act to reduce the horizontal temperature gradient by heating more at higher latitudes and shifting the heating into the middle atmosphere; both of

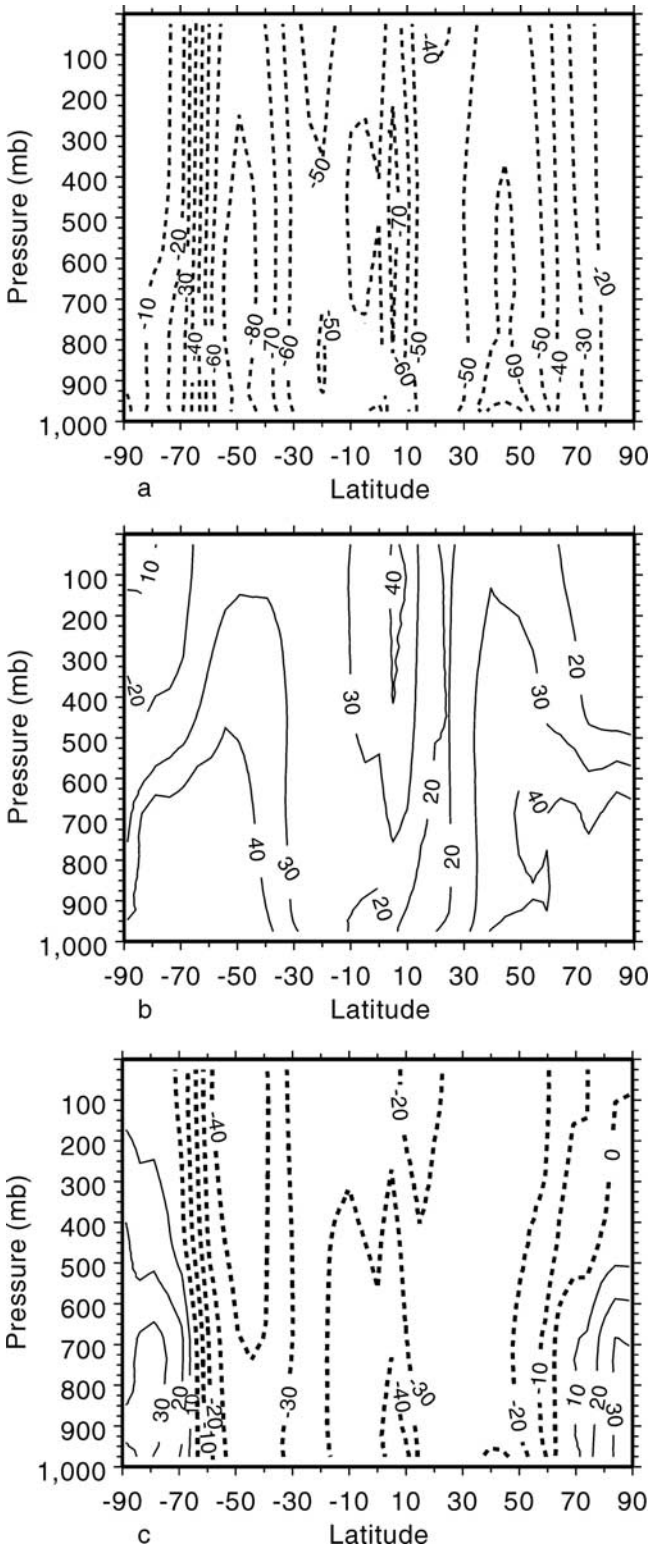


**Figure 9.** Mean pressure-latitude cross sections of the cloud effects on net fluxes in $Wm^{-2}$ (linearly interpolated from the original 5-level profiles) averaged over 1985–1989: (a) CFC-NS, (b) CFC-NL and (c) CFC-*N*. Adding these values to the clear-sky net fluxes, shown in Figure 8, gives the full-sky net fluxes.

these changes may weaken the midlatitude baroclinic waves. These results will have to be studied in more detail, separating the phases of synoptic system evolution, to determine the overall effects of clouds on the general circulation [cf. *Tselioudis et al.*, 2000].

[85] Having assembled such a detailed reconstruction of Earth's radiation budget opens up a number of lines of investigation. First, we can use this extensive data set to quantify in more detail the roles played not only by clouds but by other surface and atmospheric properties in determining the radiation budget and its variability on timescales from diurnal through decadal. Second, we can examine the particular role of each type of cloud system in altering the radiative heating of the atmosphere. Since these cloud types are characteristics of specific meteorological regimes, this is the first step toward a better understanding of how the atmospheric circulation is coupled to the radiative heating by clouds. Third, we can examine the effects of variations at different space scales–timescales on the radiative forcing of the atmospheric and oceanic circulations. Fourth, by combining the vertical profiles of radiative heating with higher-space-time-resolution information about precipitation (profiles from the Tropical Rainfall Measuring Mission [*Simpson et al.*, 1996] and later from CloudSat), we can examine the complete relationship between atmospheric motions, clouds and the total diabatic heating of the atmosphere induced by cloud processes.

[86] **Acknowledgments.** We thank B. A. Wielicki for supplying updated releases of the ERBS data sets; we thank A. Ohumra and A. Roesch for providing the BSRN data sets. We have benefited from conversations with many colleagues over the years but wish to thank especially B. E. Carlson (who also helped us with the ERBE/CERES data sets through R.-X. Ying), P. Stackhouse, B. A. Wielicki, G. Stephens, R. Stuhlmann, and E. Raschke. This work has been funded over many years by the NASA Radiation Sciences Program (now headed by H. Maring, but formerly by D. Anderson, R. Curran, and R. Schiffer). Finally, we thank the two reviewers for their responsible reviewing and helpful comments.

## References

Ackerman, T., and G. Stokes (2003), The Atmospheric Radiation Measurement Program, *Phys. Today*, *56*, 38–45.

Cairns, B., A. A. Lacis, and B. E. Carlson (1999), Absorption within inhomogeneous clouds and its parameterization in general circulation models, *J. Atmos. Sci.*, *57*, 700–714.

Chen, J., B. E. Carlson, and A. D. Del Genio (2002), Evidence for strengthening of the tropical general circulation in the 1990's, *Science*, *295*, 838–841.

Chen, T., and W. B. Rossow (2002), Determination of top-of-atmosphere longwave radiative fluxes: A comparison between two approaches using ScaRaB data, *J. Geophys. Res.*, *107*(D8), 4070, doi:10.1029/2001JD000914.

Chen, T., Y.-C. Zhang, and W. B. Rossow (2000), Sensitivity of radiative heating rate profiles to variations of cloud layer overlap, *J. Clim.*, *13*, 2941–2959.

Currey, J. C. (2002), Geolocation assessment algorithm for CALIPSO using coastline detection, *NASA Tech. Pap., TP-2002-211956*, 22 pp.

Curry, J. A., et al. (2004), SEAFLUX, *Bull. Am. Meteorol. Soc.*, *85*, 409–424.

Gaffen, D. J., and W. P. Elliott (1993), Column water vapor content in clear and cloudy skies, *J. Clim.*, *6*, 2278–2287.

Gordon, H. R., and M. Wang (1994), Influence of oceanic whitecaps on atmospheric correction of SeaWiFS, *Appl. Opt.*, *33*, 7754–7763.

Han, Q., W. B. Rossow, and A. A. Lacis (1994), Near-global survey of effective droplet radii in liquid water clouds using ISCCP data, *J. Clim.*, *7*, 465–497.

Han, Q., W. B. Rossow, J. Chou, K.-S. Kuo, and R. M. Welch (1999), The effects of aspect ratio and surface roughness on satellite retrievals of ice-cloud properties, *J. Quant. Spectrosc. Radiat. Trans.*, *63*, 559–583.

Hansen, J., and M. Sato (2001), Trends of measured climate forcing agents, *Proc. Natl. Acad. Sci. U. S. A.*, *98*(26), 14,778–14,783.

Hansen, J., G. Russell, D. Rind, P. Stone, A. Lacis, S. Lebedeff, R. Ruedy, and L. Travis (1983), Efficient three-dimensional global models for climate studies: Model I and II, *Mon. Weather Rev.*, *111*, 609–662.

Hansen, J., et al. (2002), Climate forcings in Goddard Institute for Space Studies SI2000 simulations, *J. Geophys. Res.*, *107*(D18), 4347, doi:10.1029/2001JD001143.

Jain, A. K., B. P. Briegleb, K. Minschwaner, and D. J. Wuebbles (2000), Radiative forcings and global warming potentials for 39 greenhouse gases, *J. Geophys. Res.*, *105*, 20,773–20,790.

Kalnay, E., et al. (1996), The NCEP/NCAR 40-year reanalysis project, *Bull. Am. Meteorol. Soc.*, *77*, 437–471.

Kidwell, K. (1995), *NOAA Polar Orbiter Data Products Users Guide*, 304 pp., Natl. Environ. Satell., Data and Inf. Serv., Silver Spring, Md.

Koch, D. (2001), Transport and direct radiative forcing of carbonaceous and sulfate aerosols in the GISS GCM, *J. Geophys. Res.*, *106*, 20,311–20,332.

Koch, D., D. Jacob, I. Tegen, D. Rind, and M. Chin (1999), Tropospheric sulfur simulation and sulfate direct radiative forcing in the GISS GCM, *J. Geophys. Res.*, *104*, 23,799–23,822.

Lau, N.-C., and M. W. Crane (1995), A satellite view of the synoptic-scale organization of cloud properties in midlatitude and tropical circulation systems, *Mon. Weather Rev.*, *123*, 1984–2006.

Lau, N.-C., and M. W. Crane (1997), Comparing satellite and surface observations of cloud patterns in synoptic-scale circulation systems, *Mon. Weather Rev.*, *125*, 3172–3189.

Levine, J. S. (Ed.) (1996), *Biomass Burning and Global Change*, vol. 1, MIT Press, Cambridge, Mass.

Liao, X., and D. Rind (1997), Local upper tropospheric/lower stratospheric clear-sky water vapor and tropospheric deep convection, *J. Geophys. Res.*, *102*, 19,543–19,557.

Loeb, N. G., N. Manalo-Smith, K. Loukachine, S. Kato, and B. A. Wielicki (2002), A new generation of angular distribution models for top-of-atmosphere radiative flux estimation from the Clouds and the Earth's Radiant Energy System (CERES) satellite instrument, paper presented at 11th Conference on Atmospheric Radiation, Am. Meteorol. Soc., Ogden, Utah, 3 –7 June.

Loeb, N. G., S. Kato, N. Manalo-Smith, S. K. Gupta, W. F. Miller, P. Minnis, and B. A. Wielicki (2003), Angular distribution models for top-of-atmosphere radiative flux estimation from the Clouds and the Earth's Radiant Energy System instrument on the tropical rainfall measuring mission satellite, Part I: Methodology, *J. Appl. Meteorol.*, *42*, 240–265.

Loukachine, K., N. G. Loeb, and N. Manalo-Smith (2002), Validation of top-of-atmosphere longwave radiative flux estimates from Clouds and the Earth's Radiant Energy System (CERES) angular distribution models, paper presented at 11th Conference on Atmospheric Radiation, Am. Meteorol. Soc., Ogden, Utah, 3 –7 June.

Luo, Z., W. B. Rossow, T. Inoue, and C. J. Stubenrauch (2002), Did the eruption of the Mt. Pinatubo volcano affect cirrus properties?, *J. Clim.*, *15*, 2806–2820.

Ma, Q., and R. H. Tipping (1991), A far-wing line shape theory and its application to the water continuum absorption in the infrared region, 1, *J. Chem. Phys.*, *95*, 6290–6301.

Machado, L. A. T., and W. B. Rossow (1993), Structural characteristics and radiative properties of tropical cloud clusters, *Mon. Weather Rev.*, *121*, 3234–3260.

Matthews, E. (1984), Prescription of land-surface boundary condition in GISS GCM II: A simple method based on high-resolution vegetation data bases, *NASA Tech. Memo., 86096*, 20 pp.

McPeters, R. D., P. K. Bhartia, A. J. Krueger, and J. R. Herman (1996), Nimbus-7 Total Ozone Mapping Spectrometer (TOMS) data products user's guide, *NASA Ref. Publ.*, *1384*.

Minschwaner, K., R. W. Carver, B. P. Briegleb, and A. E. Roche (1998), Infrared radiative forcing and atmospheric lifetimes of trace species based on observations from UARS, *J. Geophys. Res.*, *103*, 23,243–23,253.

Mishchenko, M. I., W. B. Rossow, A. Macke, and A. A. Lacis (1996a), Sensitivity of cirrus cloud albedo, bidirectional reflectance, and optical thickness retrieval to ice-particle shape, *J. Geophys. Res.*, *101*, 16,973–16,985.

Mishchenko, M. I., L. D. Travis, and D. W. Mackowski (1996b), T-matrix computations of light scattering by nonspherical particles: A review, *J. Quant. Spectrosc. Radiat. Transfer*, *55*, 535–575.

Naik, V., A. K. Jain, K. O. Patten, and D. J. Wuebbles (2000), Consistent sets of atmospheric lifetimes and radiative forcings on climate for CFC replacements: HCFCs and HFCs, *J. Geophys. Res.*, *105*, 6903–6914.

Ohmura, A., and H. Gilgen (1991), The GEBA data base, interactive applications, retrieving data, *Rep. 2*, 60 pp., Global Energy Balance Arch., World Clim. Program Water Proj. A7, Zürich.

Ohmura, A., and H. Gilgen (1992), Global Energy Balance Archive (GEBA, WCP-Eater A7) and new aspects of the global radiation distribution on the Earth's surface, in *IRS '92: Current Problems in Atmospheric Radiation*, edited by S. Keevallik and O. Kärner, pp. 271–274, A. Deepak, Hampton, Va.

Ohmura, A., et al. (1998), Baseline Surface Radiation Network (BSRN/WCRP): New precision radiometry for climate research, *Bull. Am. Meteorol. Soc.*, *79*, 2115–2136.

Oinas, V., A. A. Lacis, D. Rind, D. T. Shindell, and J. E. Hansen (2001), Radiative cooling by stratospheric water vapor: Big differences in GCM results, *Geophys. Res. Lett.*, *28*, 2791–2794.

Oort, A. H. (1983), *Global Atmospheric Circulation Statistics, 1958–1973*, *NOAA Prof. Pap. 14*, 180 pp. + 47 microfiches, U.S. Govt. Print. Off., Washington, D. C.

Poore, K., J.-H. Wang, and W. B. Rossow (1995), Cloud layer thickness from a combination of surface and upper-air observations, *J. Clim.*, *8*, 550–558.

Prigent, C., F. Aires, and W. B. Rossow (2003), Land surface skin temperatures from a combined analysis of microwave and infrared satellite observations for an all-weather evaluation of the differences between air and skin temperatures, *J. Geophys. Res.*, *108*(D10), 4310, doi:10.1029/2002JD002301.

Ramanathan, V., R. D. Cess, E. F. Harrison, P. Minnis, B. R. Barkstrom, E. Ahmad, and D. Hartmann (1989), Cloud-radiative forcing and climate: Results from the Earth Radiation Budget Experiment, *Science*, *243*, 57–63.

Rind, D., and X. Liao (1997), Stratospheric Aerosol and Gas Experiment II CD-ROM atlas of global mean monthly mean aerosols, ozone, $NO_2$, water vapor, and relative humidity (1985–1993), *Earth Interact.*, *1*, paper 2, doi:10.1175/1087-3562(1997)001.

Rind, D., and W. B. Rossow (1984), The effects of physical processes on the Hadley circulation, *J. Atmos. Sci.*, *41*, 479–507.

Roberts, R. E., J. E. A. Selby, and L. M. Biberman (1976), Infrared continuum absorption by atmospheric water vapor in the 8–12 μm window, *Appl. Opt.*, *15*, 2085–2090.

Rossow, W. B., and L. C. Garder (1993), Validation of ISCCP cloud detections, *J. Clim.*, *6*, 2370–2393.

Rossow, W. B., and A. A. Lacis (1990), Global, seasonal cloud variation from satellite radiance measurements, 2, Cloud properties and radiative effects, *J. Clim.*, *3*, 1204–1253.

Rossow, W. B., and R. A. Schiffer (1991), ISCCP cloud data products, *Bull. Am. Meteorol. Soc.*, *72*, 2–20.

Rossow, W. B., and R. A. Schiffer (1999), Advances in understanding clouds from ISCCP, *Bull. Am. Meteorol. Soc.*, *80*, 2261–2287.

Rossow, W. B., and Y.-C. Zhang (1995), Calculation of surface and top of atmosphere radiative fluxes from physical quantities based on ISCCP data sets: 2. Validation and first results, *J. Geophys. Res.*, *100*, 1167–1197.

Rossow, W. B., A. W. Walker, D. Bueschel, and M. Roiter (1996), International Satellite Cloud Climatology Project (ISCCP) documentation of new cloud datasets, *WMO/TD-737*, 115 pp., World Clim. Res. Programme, Geneva, Feb.

Rossow, W. B., C. Delo, and B. Cairns (2002), Implications of the observed mesoscale variations of clouds for the Earth's radiation budget, *J. Clim.*, *15*, 557–585.

Simpson, J., C. Kummerow, W. K. Tao, and R. F. Adler (1996), On the Tropical Rainfall Measuring Mission (TRMM), *Meteorol. Atmos. Phys.*, *60*, 19–36.

Stephens, G. L., et al. (2002), The CloudSat mission and the A-Train: A new dimension of space-based observations of clouds and precipitation, *Bull. Am. Meteorol. Soc.*, *83*, 1771–1790.

Stubenrauch, C. J., W. B. Rossow, N. A. Scott, and A. Chedin (1999), Clouds as seen by satellite sounders (3I) and imagers (ISCCP): III. Combining 3I and ISCCP cloud parameters for better understanding of cloud radiative effects, *J. Clim.*, *12*, 3419–3442.

Tegen, I., and A. A. Lacis (1996), Modeling of particle size distribution and its influence on the radiative properties of mineral dust aerosol, *J. Geophys. Res.*, *101*, 19,237–19,244.

Tegen, I., D. Koch, A. A. Lacis, and M. Sato (2000), Trends in tropospheric aerosol loads and corresponding impact on direct radiative forcing between 1950 and 1990: A model study, *J. Geophys. Res.*, *105*, 26,971–26,989.

Tipping, R. H., and Q. Ma (1995), Theory of the water vapor continuum and validations, *Atmos. Res.*, *36*, 69–94.

Tselioudis, G., Y.-C. Zhang, and W. B. Rossow (2000), Cloud and radiation variations associated with northern midlatitude low and high sea level pressure regimes, *J. Clim.*, *13*, 312–327.

U.S. Department of Commerce (1987), NMC format for observational data, office note 29, NOAA Natl. Weather Serv. Natl. Meteorol. Cent., Camp Springs, Md.

Wang, J., and W. B. Rossow (1998), Effects of cloud vertical structure on atmospheric circulation in the GISS GCM, *J. Clim.*, *11*, 3010–3029.

Wang, J., W. B. Rossow, T. Uttal, and M. Rozendaal (1999), Variability of cloud vertical structure during ASTEX from a combination of rawinsonde, radar, ceilometer and satellite data, *Mon. Weather Rev.*, *127*, 2484–2502.

Wang, J., W. B. Rossow, and Y.-C. Zhang (2000), Cloud vertical structure and its variations from 20-yr global rawinsonde dataset, *J. Clim.*, *12*, 3041–3056.

Webster, P. J., C. A. Clayson, and J. A. Curry (1996), Clouds, radiation, and the diurnal cycle of sea surface temperature in the tropical western Pacific, *J. Clim.*, *9*, 1717–1730.

Whitlock, C. H., J. E. Hay, D. A. Robinson, S. K. Cox, D. I. Wardle, and S. R. LeCroy (1990a), Downward shortwave surface irradiance from 17 sites for the FIRE/SRB Wisconsin experiment from October 12 through November 2, *NASA Tech. Memo., 102596*, 272 pp.

Whitlock, C. H., S. K. Cox, and S. R. LeCroy (1990b), Downwelled longwave surface irradiance data from five sites for the FIRE/SRB Wisconsin experiment from October 12 through November 2, *NASA Tech. Memo., 102597*, 187 pp.

Wielicki, B. A., B. R. Barkstrom, E. F. Harrison, R. B. Lee, G. L. Smith, and J. E. Cooper (1996), Clouds and the Earth's Radiant Energy System (CERES): An Earth Observing System experiment, *Bull. Am. Meteorol. Soc.*, *77*, 853–868.

Wielicki, B. A., et al. (2002), Evidence for large decadal variability in the tropical mean radiative energy budget, *Science*, *295*, 841–844.

Wiscombe, W. J., and S. G. Warren (1980), A model for the spectral albedo of snow, I: Pure snow, *J. Atmos. Sci.*, *37*, 2712–2733.

Young, G. S., D. V. Ledvina, and C. W. Fairall (1992), Influence of precipitating convection on the surface energy budget observed during a Tropical Ocean Global Atmosphere pilot cruise in tropical western Pacific Ocean, *J. Geophys. Res.*, *97*, 9595–9603.

Zhang, Y.-C., and W. B. Rossow (1997), Estimating meridional energy transports by the atmospheric and oceanic general circulations using boundary flux data, *J. Clim.*, *10*, 2358–2373.

Zhang, Y.-C., and W. B. Rossow (2002), New ISCCP global radiative flux data products, *GEWEX News*, *12*(4), 7.

Zhang, Y.-C., W. B. Rossow, and A. A. Lacis (1995), Calculation of surface and top of atmosphere radiative fluxes from physical quantities based on ISCCP data sets: 1. Method and sensitivity to input data uncertainties, *J. Geophys. Res.*, *100*, 1149–1165.

A. A. Lacis, M. I. Mishchenko, and W. B. Rossow, NASA Goddard Institute for Space Studies, New York, NY 10025, USA.

V. Oinas, Stinger Ghaffarian Technology, Inc., New York, NY 10025, USA.

Y. Zhang, Department of Applied Physics and Applied Mathematics, Columbia University, New York, NY 10032, USA. (yzhang@giss.nasa.gov)